Open access • Posted Content • DOI:10.1101/693671

Single cell chromatin accessibility reveals pancreatic islet cell type- and state-specific regulatory programs of diabetes risk — Source link

Joshua Chiou, Chun Zeng, Zhang Cheng, Jee Yun Han ...+14 more authors

Institutions: University of California, San Diego

Published on: 09 Jul 2019 - bioRxiv (Cold Spring Harbor Laboratory)

Topics: Chromatin, Diabetes risk, Beta cell, Epigenomics and Cell type

Related papers:

- The Sequence Alignment/Map format and SAMtools
- Model-based Analysis of ChIP-Seq (MACS)
- Fine-mapping type 2 diabetes loci to single-variant resolution using high-density imputation and islet-specific epigenome maps.
- Simple Combinations of Lineage-Determining Transcription Factors Prime cis-Regulatory Elements Required for Macrophage and B Cell Identities
- A global reference for human genetic variation.

Share this paper:

View more about this paper here: https://typeset.io/papers/single-cell-chromatin-accessibility-reveals-pancreatic-islet-1ism7qz299

bioRxiv preprint doi: https://doi.org/10.1101/693671; this version posted July 9, 2019. The copyright holder for this preprint (which was not certified by peer review) is the author/funder, who has granted bioRxiv a license to display the preprint in perpetuity. It is made available under aCC-BY-NC-ND 4.0 International license.

1 # Single cell chromatin accessibility reveals pancreatic islet cell type-
2 and state-specific regulatory programs of diabetes risk

3 Joshua Chiou*[,1], Chun Zeng*[,2,3], Zhang Cheng[4], Jee Yun Han[4], Michael Schlichting[2,3], Serina
4 Huang[2], Jinzhao Wang[2,3], Yinghui Sui[2,3], Allison Deogaygay[2], Mei-Lin Okino[2], Yunjiang Qiu[3],
5 Ying Sun[2], Parul Kudtarkar[2], Rongxin Fang[3], Sebastian Preissl[4], Maike Sander[**,#,2,3,5], David
6 Gorkin[**,#,4], Kyle J Gaulton[**,#,2,5]

7

8 1. Biomedical Graduate Studies Program, University of California San Diego, La Jolla CA
9 2. Department of Pediatrics, Pediatric Diabetes Research Center, University of California San
10 Diego, La Jolla CA
11 3. Department of Cellular and Molecular Medicine, University of California San Diego, La Jolla
12 CA
13 4. Center for Epigenomics, University of California San Diego, La Jolla CA
14 5. Institute for Genomic Medicine, University of California San Diego, La Jolla CA
15

16 * Authors contributed equally to this work
17 ** Authors jointly supervised this work
18
19 # Corresponding author:
20
21 Kyle Gaulton
22 9500 Gilman Drive, #0746
23 Department of Pediatrics
24 University of California San Diego
25 858-822-3640
26 kgaulton@ucsd.edu
27
28 David Gorkin
29 9500 Gilman Drive, #0767
30 Center for Epigenomics
31 University of California San Diego
32 858-534-7581
33 dgorkin@ucsd.edu
34
35 Maike Sander
36 9500 Gilman Drive, #0695
37 Pediatric Diabetes Research Center
38 Departments of Pediatrics & Cellular and Molecular Medicine
39 University of California San Diego
40 858-246-0843
41 masander@ucsd.edu

bioRxiv preprint doi: https://doi.org/10.1101/693671; this version posted July 9, 2019. The copyright holder for this preprint (which was not certified by peer review) is the author/funder, who has granted bioRxiv a license to display the preprint in perpetuity. It is made available under aCC-BY-NC-ND 4.0 International license.

Abstract

Genetic risk variants for complex, multifactorial diseases are enriched in *cis*-regulatory elements. Single cell epigenomic technologies create new opportunities to dissect cell type-specific mechanisms of risk variants, yet this approach has not been widely applied to disease-relevant tissues. Given the central role of pancreatic islets in type 2 diabetes (T2D) pathophysiology, we generated accessible chromatin profiles from 14.2k islet cells and identified 13 cell clusters including multiple alpha, beta and delta cell clusters which represented hormone-producing and signal-responsive cell states. We cataloged 244,236 islet cell type accessible chromatin sites and identified transcription factors (TFs) underlying both lineage- and state-specific regulation. We measured the enrichment of T2D and glycemic trait GWAS for the accessible chromatin profiles of single cells, which revealed heterogeneity in the effects of beta cell states and TFs on fasting glucose and T2D risk. We further used machine learning to predict the cell type-specific regulatory function of genetic variants, and single cell co-accessibility to link distal sites to putative cell type-specific target genes. We localized 239 fine-mapped T2D risk signals to islet accessible chromatin, and further prioritized variants at these signals with predicted regulatory function and co-accessibility with target genes. At the *KCNQ1* locus, the causal T2D variant rs231361 had predicted effects on an enhancer with beta cell-specific, long-range co-accessibility to the insulin promoter, and deletion of this enhancer reduced insulin gene and protein expression in human embryonic stem cell-derived beta cells. Our findings provide a cell type- and state-resolved map of gene regulation in human islets, illuminate likely mechanisms of T2D risk at hundreds of loci, and demonstrate the power of single cell epigenomics for interpreting complex disease genetics.

bioRxiv preprint doi: https://doi.org/10.1101/693671; this version posted July 9, 2019. The copyright holder for this preprint (which was not certified by peer review) is the author/funder, who has granted bioRxiv a license to display the preprint in perpetuity. It is made available under aCC-BY-NC-ND 4.0 International license.

72 ## Introduction
73

74 Gene regulatory programs are largely orchestrated by *cis*-regulatory elements that direct the
75 expression of genes in response to specific developmental and environmental cues. Genetic
76 variants associated with disease by genome-wide association studies (GWAS) are highly
77 enriched within putative *cis*-regulatory elements[1], highlighting the importance of regulatory
78 sequence in mediating disease risk. The activity of regulatory elements is often restricted to
79 specific cell types and/or cell states, limiting the ability of ATAC-seq and other "ensemble" (or
80 "bulk") epigenomic technologies to map regulatory elements in individual cell types within disease-
81 relevant tissues. To overcome this limitation, new approaches to obtain ATAC-seq profiles from
82 single nuclei (snATAC-seq) allow for the disaggregation of open chromatin from heterogenous
83 samples into component cell types and subtypes[2–5]. These developments create opportunities to
84 dissect the molecular mechanisms that underlie genetic risk of disease. However, to date
85 snATAC-seq data from disease-relevant human tissues are limited[6–9].

86 Type 2 diabetes (T2D) is a multifactorial disease with a highly polygenic inheritance[10]. Pancreatic
87 islets are central to genetic risk of T2D, as evidenced by shared association between T2D risk
88 and quantitative measures of islet function[11–13] and enrichment of T2D risk variants in islet
89 regulatory sites[14–18]. Islets are comprised of multiple endocrine cell types with distinct functions[19–
90 21] and are heterogeneous[22–24] in gene expression and other molecular signatures which likely
91 reflect different functional cell states[22,25,26]. Heterogeneity in the epigenome of islet cell types has
92 not been described, however, which is necessary to understand islet regulation and interpret the
93 molecular mechanisms of non-coding T2D risk variants. In this study, we map accessible
94 chromatin profiles of individual islet cells using snATAC-seq, define the regulatory programs of
95 islet cell types and cell states, describe their relationship to T2D risk and fasting glycemia, and
96 predict the molecular mechanisms of T2D risk variants.

97

98 ## Results
99

100 ### Islet snATAC-seq reveals 13 cell clusters with distinct regulatory landscapes

101 To map the accessible chromatin landscape of single islet cells, we performed snATAC-seq on
102 human pancreatic islets from three donors (Supplementary Table 1). We used a combinatorial
103 barcoding snATAC-seq approach previously optimized by our group for use on tissues[2,4] (see
104 Methods). To confirm library quality, we first analyzed the data as ensemble ATAC-seq by

bioRxiv preprint doi: https://doi.org/10.1101/693671; this version posted July 9, 2019. The copyright holder for this preprint (which was not certified by peer review) is the author/funder, who has granted bioRxiv a license to display the preprint in perpetuity. It is made available under aCC-BY-NC-ND 4.0 International license.

105 aggregating all high-quality mapped reads irrespective of barcode. Ensemble snATAC-seq from
106 all three samples showed the expected insert size distribution (Supplementary Figure 1a), strong
107 enrichment of signal at transcription start sites (TSS) (Supplementary Figure 1b), and high
108 concordance of signal with published islet ATAC-seq data[14,27–29] (Supplementary Figure 1c).

109 To obtain a collection of high-quality single cell profiles, we first filtered out cells with less than
110 1,000 reads (Supplementary Figure 1d), resulting in a total of 17,995 cells across the three
111 samples. We then clustered accessible chromatin profiles from these cells, making key
112 modifications to previous approaches (see Methods for details)[4]. First, as the inputs to clustering
113 we used normalized read counts in 5 kb sliding windows genome-wide rather than read counts
114 within ensemble peak calls, reasoning that ensemble peak calls could be biased towards more
115 common cell types. Second, we performed an initial round of clustering and quality control on a
116 per-sample basis, which removed 2,709 cells in low read depth clusters. Third, prior to clustering
117 cells across samples, we used mutual nearest neighbors[30] to correct for variability across donors.
118 Finally, we clustered all cells together and performed additional quality control by removing one
119 cluster without representation from all donors (694 cells), and one with aberrant read depth and
120 low intra-cluster similarity (192 cells). After all clustering and filtering steps, we retained 14,239
121 cells which mapped to 13 clusters, all of which had consistent representation across samples and
122 read depth profiles (Figure 1a, Supplementary Figure 2a-c).

123 To determine the cell type represented by each cluster, we examined chromatin accessibility at
124 the promoter region of the cognate hormone genes for endocrine cells and known marker genes
125 for non-endocrine cell types. Based on these marker gene promoters, we identified clusters
126 representing beta (*INS-IGF2/*insulin), alpha (*GCG/*glucagon), delta (*SST/*somatostatin), gamma
127 (*PPY*/pancreatic polypeptide) cells, exocrine acinar and ductal (labeled as ‘exocrine’; *REG1A,*
128 *S100A14*)[31,32], immune (*PTPN22*)[32], stellate (*PDGFRB*)[32], glial (*CDH19*)[33], and endothelial
129 (*CD93*)[34] cells (Figure 1b-c, Supplementary Figure 2d). We defined a broader set of marker gene
130 promoters for each cluster by identifying gene promoters with differential accessibility across
131 clusters and retaining the top 100 differential promoters for each cluster (see Methods,
132 Supplementary Table 2). To validate the cell type we assigned to each cluster, we derived gene
133 expression marker genes from published islet scRNA-seq data[23] and correlated t-statistics of
134 snATAC-seq marker gene promoters with t-statistics of scRNA-seq marker genes (see Methods,
135 Supplementary Figure 3a-e). We observed highly specific correlations between marker genes of
136 endocrine and other pancreatic cell types in snATAC-seq and scRNA-seq (Figure 1d). Of note,

bioRxiv preprint doi: https://doi.org/10.1101/693671; this version posted July 9, 2019. The copyright holder for this preprint (which was not certified by peer review) is the author/funder, who has granted bioRxiv a license to display the preprint in perpetuity. It is made available under aCC-BY-NC-ND 4.0 International license.

137 the multiple clusters of alpha, beta, and delta cells in snATAC-seq each had strongest correlation
138 with their respective cell type.

139 To characterize the regulatory programs of each cell type, we aggregated reads for cells within
140 each cluster and identified accessible chromatin sites for the cluster using MACS2 (see Methods).
141 In total we identified 244,236 accessible chromatin sites merged across the 13 clusters
142 (Supplementary Data 1), which were concordant with sites identified in ensemble islets
143 (Supplementary Figure 4a-b). Notably, accessible chromatin in alpha and beta cells was highly
144 concordant with bulk ATAC-seq of corresponding FACS-sorted populations[35,36], confirming that
145 we identified cell type-specific islet chromatin (Supplementary Figure 4c). To next understand the
146 regulatory logic underlying islet cell types, we used chromVAR[37] to identify TF sequence motifs
147 from JASPAR[38] enriched within accessible chromatin of each cell. We focused on 111 TF motifs
148 with evidence for variability across cells (see Methods, Supplementary Figure 4d, Supplementary
149 Table 3). Analysis of motif enrichments averaged across cells for each cell type revealed distinct
150 patterns of motif enrichment across cell types, many consistent with known functions in islet cells
151 (Figure 1e, Supplementary Table 3). For example, the PDX1 motif was enriched in beta
152 (normalized enrichment=0.93) and delta (1.0) cells[39], and MAF motifs were enriched in alpha (1.0)
153 and beta cells (0.93)[40–42] (Figure 1e). We also identified motif enrichments shared across all
154 endocrine cell types, such as FOXA, and in non-endocrine cell types, including IRF for immune[43]
155 (1.0) and ETS for endothelial[44] (1.0) cells (Figure 1e). Hierarchical clustering of cell types based
156 on TF motif enrichment patterns further revealed that regulatory programs of beta and delta cells
157 were closely related as were the programs of alpha and gamma cells (Figure 1e), consistent with
158 single cell expression data[31,32,45].

159

160 **Heterogeneity in islet endocrine cell accessible chromatin and regulatory programs**

161 A major strength of single cell approaches is the ability to reveal heterogeneity within a cell type.
162 Indeed, our initial clustering showed that alpha, beta and delta cells segregated into sub-clusters.
163 To characterize these sub-clusters, we determined gene promoter accessibility in each sub-
164 cluster and identified promoters with variable accessibility between sub-clusters (see Methods,
165 Supplementary Data 2). We focused on alpha and beta cells, where cell numbers allowed for
166 robust calculations. Notably, we found *INS* among genes with the most variable promoter
167 accessibility between beta cell sub-clusters (*INS-IGF2* beta OR=5.05, two-sided Fisher's exact
168 $P=3.98\times10^{-37}$), leading us to rename the beta 1 and beta 2 clusters as INS^{high} and INS^{low} beta
169 cells, respectively (Figure 1b-c; Figure 2a). Similarly, *GCG* promoter accessibility was highly

bioRxiv preprint doi: https://doi.org/10.1101/693671; this version posted July 9, 2019. The copyright holder for this preprint (which was not certified by peer review) is the author/funder, who has granted bioRxiv a license to display the preprint in perpetuity. It is made available under aCC-BY-NC-ND 4.0 International license.

170 variable between alpha cell sub-clusters (*GCG* alpha OR=3.30, P=4.68x10^{-25}), and we renamed
171 the alpha 1 and alpha 2 sub-clusters as GCG^{high} and GCG^{low} alpha cells, respectively (Figure 1b-
172 c; Figure 2a).

173 Apart from *INS* and *GCG*, we found significant overlap in the genes that distinguish hormone-high
174 (INS^{high}, GCG^{high}) from hormone-low (INS^{low}, GCG^{low}) alpha and beta cells by gene set enrichment
175 analysis (GSEA) (Figure 2b). Genes with increased promoter accessibility in hormone-high states
176 including *GCK, ABCC8, G6PC2* and *SLC30A8* were enriched for processes such as hormone
177 secretion and glucose response (Figure 2a,c, Supplementary Table 4). In contrast, genes with
178 increased promoter accessibility for hormone-low states including *ATF3*, *FOSL1*, and *FOSL2* and
179 were enriched for stress-induced signaling response[46] (Figure 2a,c, Supplementary Table 4).
180 Similar states were also evident in delta cells, although low cell numbers impede deeper analysis
181 in our study (Supplementary Figure 5). We compared genes with significantly different promoter
182 accessibility between states to gene sets describing beta cell heterogeneity (β-sub.1-4) from a
183 previous scRNA-seq study[23]. Genes with increased promoter accessibility in hormone-low cells
184 (INS^{low}, GCG^{low}) were enriched in a beta cell sub-cluster (β-sub.4) associated with ER stress and
185 protein folding and with low *INS* expression, whereas genes with increased promoter accessibility
186 in hormone-high cells (INS^{high}, GCG^{high}) were enriched in the other beta cell sub-clusters (β-sub.1-
187 3) (Figure 2b). These data reveal epigenomic differences between endocrine cell states among
188 genes involved in hormone production and stress-induced signaling responses, and point to an
189 underlying commonality in the genes that govern state-specific functions across different
190 endocrine cell types.

191 The transcriptional regulatory programs driving functional heterogeneity in alpha and beta cells
192 are unknown. Therefore, we determined TF sequence motifs differentially enriched across alpha
193 and beta cell states. We focused on 111 TF motifs showing evidence for variable enrichment
194 between alpha and beta cell states (see Methods, Supplementary Figure 6a, Supplementary
195 Table 5) and observed clear patterns that distinguished different states within alpha and beta
196 cells, again revealing commonalities across cell types (Figure 2d). For example, motifs for RFX
197 family members were enriched in hormone-high states (GCG^{high}, INS^{high}), but not in hormone-low
198 states (GCG^{low}, INS^{low}) (RFX3 - mean INS^{high} enrich=.26, INS^{low}=-.62, P=3.5x10^{-158}; GCG^{high}=.29,
199 GCG^{low}=-.56, P=7.3x10^{-91}) (Figure 2d). In contrast, motifs for FOS and JUN family members were
200 prominently enriched in hormone-low states, but not the hormone-high states (FOS::JUN - mean
201 INS^{high} enrich=-1.45, INS^{low}=4.50, P=4.7x10^{-307}; GCG^{high}=-1.45, GCG^{low}=4.46, P=2.3x10^{-292})

bioRxiv preprint doi: https://doi.org/10.1101/693671; this version posted July 9, 2019. The copyright holder for this preprint (which was not certified by peer review) is the author/funder, who has granted bioRxiv a license to display the preprint in perpetuity. It is made available under aCC-BY-NC-ND 4.0 International license.

202 (Figure 2d). Again, we also observed similar motif enrichment patterns between delta cell states
203 (Supplementary Figure 6a-b).

204 Analysis of single cells ordered along a trajectory has been used to examine gene regulatory
205 programs as a continuum rather than as discrete or binary states[6,23,47]. To explore potential
206 gradations among alpha and beta cells, we used Cicero[6] to order alpha and beta cells along
207 trajectories based on chromatin accessibility. We ordered cells using high promoter accessibility
208 at *INS* (beta) or *GCG* (alpha) as the root states for each trajectory (see Methods). We refer to the
209 axis of these trajectories as “pseudo-state” rather than the conventional “pseudo-time”, because
210 the heterogeneity appears to be more related to cell state than to time. We observed cells on a
211 gradient between hormone-high and hormone-low states of alpha and beta cells, and we noted a
212 discernable transition point within the trajectory (Figure 2e, Supplementary Figure 7a-b). These
213 trajectories allowed us to examine gene promoter accessibility and TF motif enrichment as a
214 function of pseudo-state (Figure 2e, Supplementary Figure 7c). Consistent with the above results,
215 lineage-specifying genes and enrichments for motifs in TF families such as RFX, Neurogenin-
216 ATO and NFAT decreased along the trajectory from hormone-high to -low cells, whereas
217 enrichment for motifs in TF families such as FOS/JUN, XBP and CCAAT (NFYA) increased along
218 the trajectory (Figure 2e).

219 Structurally-related TFs often have similar motifs, and thus to assign motifs to specific TFs we
220 correlated promoter-accessibility of TFs within the structural subfamily with motif enrichments
221 across the state trajectory (see Methods)[48]. Motif enrichment for the FOS/JUN family correlated
222 with the promoter accessibility of *FOSL1, FOSL2* and *JUND* across cells (Figure 2f), supporting
223 a role for these specific TFs in hormone-low cell regulation. Similarly, motif enrichment for the
224 Neurogenin-ATO subfamily correlated with promoter accessibility of *NEUROD1,* supporting a role
225 for this TF in hormone-high cell regulation (Supplementary Figure 8a). While we did not observe
226 strong correlations between RFX motif enrichment and promoter accessibility of *RFX* genes, the
227 overall high promoter accessibility of *RFX6* and *RFX3* and known function in endocrine cells[49–51]
228 suggests they are TFs likely involved in hormone-high cell regulation (Supplementary Figure 8b).

229

230 **Enrichment of islet cell type- and state-specific regulatory sequences for diabetes- and**
231 **fasting glycemia-associated genetic variants**

232 Variants associated with complex diseases and physiological traits are enriched within *cis*-
233 regulatory sequences[1,52]. More specifically, genetic variants influencing diabetes and fasting

bioRxiv preprint doi: https://doi.org/10.1101/693671; this version posted July 9, 2019. The copyright holder for this preprint (which was not certified by peer review) is the author/funder, who has granted bioRxiv a license to display the preprint in perpetuity. It is made available under aCC-BY-NC-ND 4.0 International license.

234 glucose level are enriched in pancreatic islet regulatory elements[15–17,53]. However, these
235 enrichments based on ensemble data obscure the potential role of islet cell type- and state-
236 specific regulation in these traits. Using our islet cell type- and state-resolved accessible
237 chromatin profiles, we sought to determine the enrichment of genetic variants associated with
238 type 1 and 2 diabetes[10,54] and diabetes-related quantitative phenotypes[13,55–59] as well as other
239 complex traits and disease for calibration[60–67]. We first determined the enrichment of variants in
240 accessible chromatin sites for each islet cell type and state using stratified LD score regression[68,69]
241 (see Methods). We observed significant enrichment (FDR<.1) of fasting glucose (FG) level and
242 T2D association for both INS^{high} and INS^{low} beta cell states (T2D INS^{high} Z=4.45 q-value=.001,
243 INS^{low} Z=4.00 q=.004; FG INS^{high} Z=3.93 q=.004, INS^{low} Z=3.34 q=.027), as well as enrichment of
244 body-mass index (BMI) for SST^{high} delta cells (Z=3.50 q=.027) (Figure 3a). We also observed
245 suggestive enrichment (P<.01) of 2hr glucose level adjusted for BMI for both alpha cell states
246 (GCG^{high} Z=2.45 P=.007, GCG^{low} Z=2.40 P=.008), and T2D and fasting proinsulin level for GCG^{low}
247 alpha cells (PI: Z=2.64, P=.004; T2D: Z=2.40 P=.008), although these enrichments did not pass
248 multiple test correction.

249 In these analyses, we again noted evidence for differences in enrichments between the hormone-
250 high and -low states of endocrine cells (Figure 3a). To further resolve the heterogeneity of genetic
251 association enrichment patterns, we used a novel framework to test the enrichment of genetic
252 association signal genome-wide within accessible chromatin profiles of single cells (see
253 Methods). We applied this approach to genetic association data for T2D and fasting glucose level,
254 as well as negative control traits major depressive disorder and systemic lupus erythematosus
255 (Figure 3b). We observed marked heterogeneity among beta cells in enrichment estimates for
256 fasting glucose-associated variants, whereby cells in the INS^{high} state had significantly stronger
257 enrichment than cells in the INS^{low} state (INS^{high} median Z=2.42, INS^{low} median Z=1.13, $P<2.2\times10^{-16}$
258) (Figure 3b). We further examined heterogeneity by calculating the average enrichment
259 estimates for cells binned across the 'pseudo-state' trajectory (see Figure 2), which revealed a
260 clear pattern of decreasing enrichment for fasting glucose-associated variation across pseudo-
261 state moving from INS^{high} to INS^{low} beta cells (Figure 3b). Conversely, for T2D we observed
262 enrichment for beta cells that was more consistent across INS^{high} and INS^{low} beta cells, as well as
263 across the pseudo-state trajectory (INS^{high} median Z=0.48, INS^{low} median Z=0.51, P=0.84) (Figure
264 3b). In comparison, major depressive disorder and lupus showed no evidence for enrichment for
265 beta cells (all median Z<.001) (Figure 3b). Knowledge of state-specific effects of cell types on
266 specific phenotypes can then inform interpretation of association signals for those phenotypes;
267 for example, at the *DGKB* locus, variants associated with both fasting glucose level and T2D

bioRxiv preprint doi: https://doi.org/10.1101/693671; this version posted July 9, 2019. The copyright holder for this preprint (which was not certified by peer review) is the author/funder, who has granted bioRxiv a license to display the preprint in perpetuity. It is made available under aCC-BY-NC-ND 4.0 International license.

268 overlapped a chromatin site with higher activity in INS^{high} beta cells, implicating this state-
269 dependent regulatory sequence in mediating the association signal (Figure 3c).

270 Given our ability to map both complex trait and TF motif enrichments to single cells, we reasoned
271 that joint analysis of these data could provide insights into TFs and regulatory networks through
272 which genetic effects on these traits are mediated. We correlated single cell fasting glucose level
273 and T2D enrichment z-scores with single cell TF motif enrichments from chromVAR[37], both across
274 all 14.2k islet cells as well as just the 7.2k beta cells (see Methods). Across all 14.2k cells, we
275 observed strong positive correlation between fasting glucose level and T2D enrichment and beta
276 cell lineage-specifying TF motifs (e.g. PDX1), and negative correlation with TF motifs regulating
277 other islet cell types (Figure 3d, Supplementary Figure 9, Supplementary Table 6). When next
278 considering only the 7.2k beta cells, we observed the strongest positive correlation between
279 fasting glucose level and motifs in TF families enriched for INS^{high} beta cells (from Figure 2) such
280 as RFX (ρ=.12, P=2.58x10^{-24}), FOXA (ρ=.11, P=5.41x10^{-19}), and MAF (ρ=.14, P=5.36x10^{-32}), and
281 negative correlation with INS^{low} beta cell TF motifs such as FOS/JUN and ATF (JUND ρ=-.23,
282 P=1.23x10^{-85}, ATF4 ρ=-.12, P=1.18x10^{-23}) (Figure 3d, Supplementary Table 6). Interestingly, for
283 T2D, both the strongest positive and negative correlations included motifs for TF families enriched
284 in INS^{low} beta cell such as CCAAT and CREB (NFYA ρ=.073, P=1.72x10^{-9}, CREB1 ρ=.053,
285 P=7.44x10^{-6}) and FOS/JUN (FOS::JUN ρ=-.06, P=2.45x10^{-6}) (Supplementary Figure 9,
286 Supplementary Table 6). Together these results provide state-resolved insight into the role of beta
287 cells and beta cell TFs in T2D risk and fasting glucose level.

288

289 **Genome-wide predictions of variant effects on islet cell type- and state-specific regulatory**
290 **sequence**

291 Predicting the effects of non-coding genetic variants on regulatory activity remains a major
292 challenge, in large part because the sequence vocabularies that encode regulatory function differ
293 between cell types and states. Our cell type- and state-resolved accessible chromatin profiles
294 provided an ideal opportunity to apply machine learning to model these regulatory vocabularies
295 and use these models to predict the effects of genetic variants on putative regulatory sequences.
296 We therefore used deltaSVM[70] to predict the effects of genetic variants from the Haplotype
297 Reference Consortium panel[71] on chromatin accessibility in each endocrine cell type and cell state
298 (see Methods). We identified 543,537 variants genome-wide with predicted allelic effects
299 (FDR<.1), encompassing between 128k-210k variants (9.1%-14.8% of tested variants) per cell
300 type or state (Figure 4a, Supplementary Data 3).

bioRxiv preprint doi: https://doi.org/10.1101/693671; this version posted July 9, 2019. The copyright holder for this preprint (which was not certified by peer review) is the author/funder, who has granted bioRxiv a license to display the preprint in perpetuity. It is made available under aCC-BY-NC-ND 4.0 International license.

301 To validate that our predictions captured true allelic effects on islet chromatin accessibility, we
302 first compared alpha and beta cell predictions to allelic imbalance in chromatin accessibility
303 measured directly from read count data at heterozygous variants in each sample (see Methods).
304 We found significant correlations between predicted allelic effects and allelic imbalance estimates
305 for all alpha and beta cell states (GCG^{high} Spearman ρ=.261, $P=3.27\times10^{-46}$, GCG^{low} ρ=.225,
306 $P=4.38\times10^{-10}$, INS^{high} ρ=.285, $P=1.13\times10^{-53}$, INS^{low} ρ=.297, $P=2.28\times10^{-40}$) (Figure 4b). We further
307 validated five likely causal T2D variants identified in fine-mapping studies and predicted to have
308 allelic effects on beta cell chromatin using gene reporter assays in the MIN6 beta cell line. In each
309 case, reporter assays showed significant allelic effects on enhancer activity that were directionally
310 consistent with predictions (Figure 4c). We also compared predictions to chromatin accessibility
311 quantitative trait loci (caQTLs) previously identified in ensemble islet samples[72]. We observed
312 highly significant enrichment of caQTLs among variants with predicted effects on alpha or beta
313 cells (obs.=38.8%, exp.=23.6%, two-sided Fisher's exact $P=1.64\times10^{-66}$) (Figure 4d). When sub-
314 dividing predictions based on those with shared, cell type-specific (alpha, beta) or state-specific
315 (hormone-high, hormone-low) effects we observed significant enrichment of caQTLs only among
316 shared effect variants (Figure 4d), suggesting that islet caQTLs may have lower sensitivity for
317 variants with cell type- or state-specific effects.

318 We thus sought to further characterize genetic variants predicted to have cell type- and state-
319 dependent effects on islet chromatin. For each category of variants, we performed motif
320 enrichment comparing sequences around the effect allele to the non-effect allele (see Methods).
321 Variants with state-specific effects tended to disrupt motifs for TF families such as NEUROD,
322 FOXA, MAF and RFX for hormone-high states ($-\log_{10}(P)$=59.2, 56.0, 50.3, 20.6), and signaling-
323 responsive TF families such as JUN/FOS and CREB for hormone-low states ($-\log_{10}(P)$=107.6,
324 46.8) (Figure 4e). Similarly, variants with alpha or beta cell-specific effects tended to disrupt motifs
325 for lineage-defining TFs and TF families including GATA for alpha cells ($-\log_{10}(P)$=24.8), and
326 NKX6 and PDX1 for beta cells ($-\log_{10}(P)$=17.0, 13.0) (Figure 4e). In order to assign motifs to
327 specific TFs, we again examined promoter-accessibility of TFs within the structural TF subfamily[48]
328 (see Methods). For example, among GATA subfamily members only GATA6 had high promoter
329 accessibility in alpha cells (GCG^{high}: 1.00, GCG^{low}: .97, INS^{high}: .21, INS^{low}: .13), suggesting that
330 GATA6 binding is likely disrupted in alpha cells by variants affecting the GATA motif. Similarly,
331 among NKX6 subfamily members, NKX6-1 and NKX6-3 had promoter accessibility in beta cells
332 (NKX6-1 GCG^{high}: .78, GCG^{low}: .80, INS^{high}: .98, INS^{low}: 1.00; NKX6-3 GCG^{high}: 0, GCG^{low}: 0,

bioRxiv preprint doi: https://doi.org/10.1101/693671; this version posted July 9, 2019. The copyright holder for this preprint (which was not certified by peer review) is the author/funder, who has granted bioRxiv a license to display the preprint in perpetuity. It is made available under aCC-BY-NC-ND 4.0 International license.

333 INS^{high}: .18, INS^{low}: .19), and among RFX family members RFX6 had promoter accessibility in
334 hormone-high state cells (GCG^{high}: .93, GCG^{low}: .68, INS^{high}: 0.88, INS^{low}: .85) (Figure 4e).

335 Predictions of allelic effects are particularly important in interpreting the function of low frequency
336 non-coding variants, which are impractical to assay by standard approaches such as QTL
337 mapping without very large sample sizes. We thus evaluated whether our predictions could
338 prioritize lower frequency (defined as minor allele frequency [MAF]<.05) functional variants
339 involved in T2D risk. We compared T2D association at different p-value thresholds for lower
340 frequency variants with significant effects for any endocrine cell type, as well as for each cell type
341 individually, to background variants without predicted effects (see Methods). We observed
342 enrichment of genome-wide significant T2D associations among lower frequency variants with
343 predicted effects in any endocrine cell type compared to background (Figure 4f). When
344 considering effects in each cell type, we observed enrichment of T2D association among variants
345 with predicted effects in beta cells as well as delta cells, even down to sub-genome-wide
346 significant p-values (Figure 4f). We next highlighted specific low frequency, T2D risk variants with
347 predicted effects. At the *IGF2BP3* locus, rs78840640 (MAF=.02) had allelic effects on beta cell
348 chromatin (INS^{high} beta q=.0015; INS^{low} beta q=.041), and fine-mapping data supported a causal
349 role in T2D (posterior probability [PPA]=.33) (Figure 4g). We confirmed in gene reporter assays
350 that this variant affected enhancer activity where the alternate (and T2D risk) allele G had reduced
351 activity (Figure 4c). We also observed predicted effects for rare T2D variants for example
352 rs186384225 (MAF=.0037) at *TCF7L2* and rs571342427 (MAF=.0015) at *INS-IGF2*
353 (Supplementary Figure 10a-b). These results reveal that cell type-specific chromatin can provide
354 accurate functional predictions of lower frequency variants, enabling more effective interpretation
355 of genome sequence from patients and disease cohorts.

356

357 Co-accessibility links distal regulatory variants to putative target genes in distinct islet cell 358 types and states

359 Defining the genes affected by regulatory element activity remains a major challenge, as
360 enhancers can regulate gene activity over large, non-adjacent distances[73]. A number of
361 approaches have been developed to link regulatory elements to target genes including 3D
362 chromatin architecture assays and correlation of accessible chromatin activity across multiple
363 samples[74,75]. While these approaches have different strengths, a common weakness is reliance
364 on ensemble data and non-cell type-resolved information[27,76]. Recently, a new approach was
365 developed to link regulatory elements based on co-accessibility across single cells[6], which has

bioRxiv preprint doi: https://doi.org/10.1101/693671; this version posted July 9, 2019. The copyright holder for this preprint (which was not certified by peer review) is the author/funder, who has granted bioRxiv a license to display the preprint in perpetuity. It is made available under aCC-BY-NC-ND 4.0 International license.

366 the potential to provide cell type-resolved enhancer-promoter relationships. We thus sought to
367 leverage accessible chromatin profiles across thousands of islet cells to define co-accessibility
368 between sites in specific cell types. For these analyses we again focused on alpha and beta cells
369 where cell numbers (5,594 and 7,170 cells, respectively) gave us the most power to effectively
370 derive co-accessibility maps.

371 To calibrate the extent to which co-accessibility reflected physical interactions between regulatory
372 elements, we first performed a distance-matched comparison between co-accessible sites
373 stratified by co-accessibility threshold to chromatin loops identified from Hi-C and promoter
374 capture Hi-C (pcHi-C) assays in primary islets[27,76]. We observed strong enrichment for pairs of
375 sites with co-accessibility scores >.05 in both alpha and beta cells for islet chromatin loops
376 identified from pcHi-C and Hi-C compared to sites that had no evidence for co-accessibility (Figure
377 5a, Supplementary Figure 11a-c). We therefore used this threshold (.05) to define co-accessibility,
378 through which we identified 593,769 co-accessible sites in alpha cells (Supplementary Data 4)
379 and 487,549 co-accessible sites in beta cells (Supplementary Data 5). There were 64,045 (alpha)
380 and 57,374 (beta) unique distal sites co-accessible with a gene promoter (median 2 promoters
381 per site), and 19,872 (alpha) and 19,269 (beta) unique gene promoters co-accessible with a distal
382 site (median 9 per gene in alpha, 6 in beta cells) (Supplementary Figure 11d-e).

383 Among co-accessible links to gene promoters, the majority (71.9%) were alpha or beta cell-
384 specific, highlighting the value of single cell-resolved data for identifying putative cell type-specific
385 regulatory interactions. As an example of cell type-specific co-accessibility, the *PDX1* promoter
386 had co-accessibility with 35 sites in beta cells, including a site over 500 kb distal that directly
387 coincided with an islet pcHi-C loop, only 7 of which were also found in alpha cells (Figure 5b). In
388 another example, at the *ARX* locus, 17 sites were co-accessible with the *ARX* promoter in alpha
389 cells, none of which were co-accessible in beta cells (Supplementary Figure 11f). Conversely, as
390 an example of shared co-accessibility across cell types, the *NEUROD1* promoter was co-
391 accessible with 52 and 47 chromatin sites in alpha and beta cells, respectively, of which 26 were
392 shared and several were over 500 kb distal (Supplementary Figure 11g).

393 Given heterogeneity in alpha and beta cell regulatory programs, we next cataloged co-accessible
394 links between distal alpha and beta cell sites and gene promoters that had differential activity
395 across and hormone-high and -low states (see Methods). We observed 25,012 (alpha) and 9,641
396 (beta) co-accessible links where both the distal site (unique distal sites: alpha=10,926,
397 beta=7,958) and the gene promoter (unique promoters: alpha=1,951, beta=1,516) were
398 differentially active between states in the same direction. State-dependent co-accessible links

bioRxiv preprint doi: https://doi.org/10.1101/693671; this version posted July 9, 2019. The copyright holder for this preprint (which was not certified by peer review) is the author/funder, who has granted bioRxiv a license to display the preprint in perpetuity. It is made available under aCC-BY-NC-ND 4.0 International license.

399 included both gene promoters active in the hormone-high state such as *INS*, *GCG, G6PC2,* and
400 *NEUROD1*, and gene promoters active in the hormone-low state such as *FOSL1, FOSL2,*
401 *CREB1,* and *CREB5*. We also identified genes with different isoform promoters co-accessible
402 with hormone-high and hormone-low dependent distal sites such as *GLIS3* (Supplementary
403 Figure 11h), suggesting these genes have distinct regulatory programs driving isoform-specific
404 activity across different cell states.

405 Distal sites with co-accessibility links to gene promoters harbored risk variants for T2D at many
406 loci, suggesting this approach can prioritize target genes of T2D risk variants in islets. We
407 observed one such example at the *KCNQ1* locus, where an islet chromatin site located in intron
408 3 of *KCNQ1* had beta cell-specific co-accessibility with the *INS* promoter over 500 kb distal and
409 harbored a causal T2D risk variant rs231361 (PPA=1)[10]. (Figure 5c). Published 4C data from the
410 EndoC-βH1 human beta cell line[77] anchored on the *INS* promoter supported the existence of
411 physical interactions between this site and the *INS* promoter in beta cells (Supplementary Figure
412 12a). Interestingly, the site was more accessible in INS^{high} beta cells compared to INS^{low} beta
413 cells, and rs231361 was predicted to have state-specific effects on beta cell chromatin
414 accessibility (INS^{high} beta FDR q=.060; INS^{low} beta FDR q=.40). Furthermore, rs231361 disrupted
415 an *RFX* family sequence motif, which itself was enriched in the INS^{high} beta cell state (Figure 5c,
416 also see Figure 2c). The *KCNQ1* locus is also associated with quantitative measures of insulin
417 secretion[78–81] and fasting glucose level[82], suggesting that the mechanism of action of this locus
418 on T2D risk is likely mediated through beta cell function in a state-dependent manner.

419 To validate the effects of the chromatin site containing rs231361 on distal regulation of *INS* in
420 beta cells, we deleted a 2.6 kb region flanking the site in human embryonic stem cells (hESCs)
421 by CRISPR/Cas9-mediated genome editing, generating three bi-allelic deletion clones
422 (*KCNQ1*$^{\Delta Enh}$) (Figure 5c, Supplementary Figure 12b-c). We then differentiated the three
423 *KCNQ1*$^{\Delta Enh}$ clones as well as two unedited control clones into beta cells using an established
424 protocol[83] with minor modifications (see Methods). Analysis of cultures at the beta cell stage
425 revealed similar numbers of INS^{+} cells in *KCNQ1*$^{\Delta Enh}$ and control clones (91.1±4.02% vs
426 94.6±2.11%) (Supplementary Figure 12d), suggesting that the enhancer deletion had no effect
427 on beta cell differentiation. Further supporting this conclusion, similar numbers of cells expressed
428 the beta cell marker NKX6-1 in *KCNQ1*$^{\Delta Enh}$ and control cultures (Supplementary Figure 12e).
429 Likewise, *NKX6-1* mRNA levels were similar (FDR=0.98) (Supplementary Figure 12f). Next, we
430 determined effects of the enhancer deletion on gene expression in *cis,* interrogating all genes
431 within 2 Mb of the enhancer. We observed a significant decrease in the expression of *INS*

bioRxiv preprint doi: https://doi.org/10.1101/693671; this version posted July 9, 2019. The copyright holder for this preprint (which was not certified by peer review) is the author/funder, who has granted bioRxiv a license to display the preprint in perpetuity. It is made available under aCC-BY-NC-ND 4.0 International license.

432 (P=3.02x10^{-4}; FDR=0.066) and *CDKN1C* (P=1.96x10^{-4}; FDR=0.059) in *KCNQ1*$^{\Delta Enh}$ compared to
433 control cells, whereas other genes in the region showed no difference in expression (all P>.05;
434 note *KCNQ1* itself was not expressed) (Figure 5d). Analysis of INS protein by
435 immunofluorescence staining, flow cytometry, and ELISA further revealed reduced INS protein
436 abundance in *KCNQ1*$^{\Delta Enh}$ beta cells (Figure 5e-g). In contrast, beta cell NKX6-1 protein levels
437 were not affected (Supplementary Figure 12e), confirming specific effects of the enhancer
438 deletion on *INS* mRNA and protein expression in beta cells.

439

440 **A resource of islet cell type and state regulatory programs to annotate T2D risk variants**

441 Together our results provide a multi-tiered reference of islet cell type and cell state regulatory
442 programs through which non-coding genetic variants can be comprehensively annotated. As most
443 genetic risk variants for diabetes are non-coding, this resource can be used to interpret their
444 molecular mechanisms. We therefore annotated the islet cell type-specific regulatory programs
445 of T2D risk variants using fine-mapping 'credible sets' of 402 risk signals[10,84]. Fine-mapped
446 credible set variants at 239 risk signals mapped within an islet cell type chromatin site and, at 97
447 of these 239 risk signals, credible set variants also had both predicted allelic effects and co-
448 accessibility with a gene promoter (Supplementary Table 7).

449 Genes co-accessible with fine-mapped credible set T2D variants in islet cell type chromatin were
450 enriched for biological processes related to protein localization and transport, stress response,
451 cell cycle, and signal transduction (Supplementary Table 8). Co-accessible genes also included
452 numerous genes involved in monogenic diabetes such as *INS, KCNJ11, ABCC8, HNF1A,*
453 *HNF4A, GCK,* and *NKX2-2*, as well as TFs in structural families with lineage- and state-specific
454 motif enrichments (from Figures 1-2) such as *NKX6-1, NFATC2* and *RFX6*. At 22 T2D loci, fine-
455 mapped variants at multiple independent risk signals were co-accessible with the same gene,
456 providing independent support for the role of these genes in T2D. For example, at the *KCNQ1*
457 locus (11p15), fine-mapped variants at four T2D risk signals (including rs231361 above) were in
458 sites co-accessible with the *INS* promoter (Supplementary Figure 13a), and at the *CDKN2A/B*
459 locus (9p21), fine-mapped variants at five T2D signals were in sites co-accessible with the
460 *CDKN2A, MTAP* and *DMRTA1* promoters (Supplementary Figure 13b). In other examples, at the
461 *DGKB* locus (7p21), fine-mapped variants at two T2D signals were in sites co-accessible with the
462 *DGKB* promoter (Supplementary Figure 13c), and at 7p13 fine-mapped variants at two T2D
463 signals were in sites co-accessible with the *GCK* promoter (Supplementary Figure 13d).

bioRxiv preprint doi: https://doi.org/10.1101/693671; this version posted July 9, 2019. The copyright holder for this preprint (which was not certified by peer review) is the author/funder, who has granted bioRxiv a license to display the preprint in perpetuity. It is made available under aCC-BY-NC-ND 4.0 International license.

464 In order to effectively provide these data to the community to facilitate hypothesis testing and
465 mechanistic discovery, we developed a publicly-accessible web portal and database
466 (https://www.t2depigenome.org) which contains processed data and islet cell type annotations
467 generated in this study, as well as epigenomic data from islets and other diabetes-relevant tissues
468 available in other published studies (Supplementary Figure 14a-f). In addition, the portal enables
469 the user to query genetic variants for their respective islet cell type annotations.

470

471 **Discussion**

472

473 Our findings provide a roadmap demonstrating how single cell accessible chromatin data derived
474 from disease-relevant primary tissue can be utilized to define the cell types, cell states, *cis*
475 regulatory elements and genes involved in the genetic basis of complex disease. Over 400 known
476 risk signals for T2D have been identified, yet only a handful have been characterized
477 molecularly[16,18,27,85–91]. Identifying the genes affected by non-coding risk variants is paramount for
478 understanding the molecular pathways dysregulated in disease and can inform therapeutic target
479 discovery. Candidate target genes of T2D risk signals derived using single cell co-accessibility
480 were highly enriched for disease-relevant biological processes, and many of these genes serve
481 as compelling targets for mechanistic study. At the *KCNQ1* locus, co-accessibility data and hESC
482 beta cell models revealed that a long-range enhancer harboring a causal T2D variant affects
483 insulin expression and protein levels in beta cells. Mutations of *INS* cause monogenic diabetes
484 and tandem repeats in *INS* affect T1D risk[92,93], but to our knowledge *INS* has not been directly
485 implicated in T2D risk. The *KCNQ1* locus has a complex contribution to T2D with 10 signals in
486 the region that each confer independent risk[10], four of which had beta cell co-accessibility with the
487 *INS* promoter. We therefore speculate that the *KCNQ1* locus mediates T2D risk through multiple
488 long-range regulatory effects on *INS*, in addition to *CDKN1C* and other genes.

489 Single cell accessible chromatin uncovered heterogeneity in the regulatory programs of endocrine
490 cell types, revealing cell type- and state-resolved effects of genetic variants on fasting glucose
491 and T2D risk. Previous studies have characterized heterogeneity in beta cell physiological
492 function, cell surface markers, and gene expression[22,94,95]. The heterogeneity we observed in the
493 beta cell epigenome mapped to cellular states related to insulin production and stress-related
494 signaling response[23], and we identified TFs likely driving cell state-specific functions. Integrating
495 single cell heterogeneity with large-scale genetic association data revealed that genetic variants
496 modulating fasting glucose levels likely act through the insulin-producing beta cell state, whereas

bioRxiv preprint doi: https://doi.org/10.1101/693671; this version posted July 9, 2019. The copyright holder for this preprint (which was not certified by peer review) is the author/funder, who has granted bioRxiv a license to display the preprint in perpetuity. It is made available under aCC-BY-NC-ND 4.0 International license.

497 genetic risk of T2D is mediated through both the insulin-producing state and other functional beta
498 cell state(s). Moreover, given similar heterogeneity in the epigenomes of alpha and delta cells,
499 our results reveal that endocrine cell regulation involves both lineage-specific programs as well
500 as an additional layer of state-specific programs common across endocrine cell types.

501 In summary, we present the most detailed characterization of islet cell type and state regulatory
502 programs to date and a web resource to query these programs. When combined with genetic fine-
503 mapping and genome sequencing, this resource will greatly enhance efforts to define molecular
504 mechanisms of T2D risk. More broadly, our study provides a framework for using single cell
505 chromatin from disease-relevant tissues to interpret the genetics and biological mechanisms of
506 complex disease.

507

508 Methods

509

510 Islet processing and nuclei isolation

511 We obtained islet preparations from three donors for the Integrated Islet Distribution Program
512 (IIDP) (Supplementary Table 1). Islet preparations were further enriched using zinc-dithizone
513 staining followed by hand picking. Studies were given exempt status by the Institutional Review
514 Board (IRB) of the University of California San Diego.

515

516 Generation of snATAC-seq libraries

517 Combinatorial barcoding single nuclear ATAC-seq was performed as described previously[2,4] with
518 several modifications as described below. For each donor (N=3), approximately 3,000 islet
519 equivalents (IEQ, roughly 1,000 cells each) were resuspended in 1 ml nuclei permeabilization
520 buffer (10mM Tris-HCL (pH 7.5), 10mM NaCl, 3mM $MgCl_2$, 0.1% Tween-20 (Sigma), 0.1%
521 IGEPAL-CA630 (Sigma) and 0.01% Digitonin (Promega) in water) and homogenized using 1ml
522 glass dounce homogenizer with a tight-fitting pestle for 15 strokes. Homogenized islets were
523 incubated for 10 min at 4°C and filtered with 30 µm filter (CellTrics). Nuclei were pelleted with a
524 swinging bucket centrifuge (500 x g, 5 min, 4°C; 5920R, Eppendorf) and resuspended in 500 µL
525 high salt tagmentation buffer (36.3 mM Tris-acetate (pH = 7.8), 72.6 mM potassium-acetate,
526 11 mM Mg-acetate, 17.6% DMF) and counted using a hemocytometer. Concentration was
527 adjusted to 4500 nuclei/9 µl, and 4,500 nuclei were dispensed into each well of a 96-well plate.
528 Glycerol was added to the leftover nuclei suspension for a final concentration of 25 % and nuclei
529 were stored at -80°C. For tagmentation, 1 µL barcoded Tn5 transposomes[4,96] were added using

bioRxiv preprint doi: https://doi.org/10.1101/693671; this version posted July 9, 2019. The copyright holder for this preprint (which was not certified by peer review) is the author/funder, who has granted bioRxiv a license to display the preprint in perpetuity. It is made available under aCC-BY-NC-ND 4.0 International license.

530 a BenchSmart™ 96 (Mettler Toledo), mixed five times and incubated for 60 min at 37 °C with
531 shaking (500 rpm). To inhibit the Tn5 reaction, 10 µL of 40 mM EDTA were added to each well
532 with a BenchSmart™ 96 (Mettler Toledo) and the plate was incubated at 37 °C for 15 min with
533 shaking (500 rpm). Next, 20 µL 2 x sort buffer (2 % BSA, 2 mM EDTA in PBS) were added using
534 a BenchSmart™ 96 (Mettler Toledo). All wells were combined into a FACS tube and stained with
535 3 µM Draq7 (Cell Signaling). Using a SH800 (Sony), 20 nuclei were sorted per well into eight 96-
536 well plates (total of 768 wells) containing 10.5 µL EB (25 pmol primer i7, 25 pmol primer i5, 200
537 ng BSA (Sigma), PMID: 29434377). Preparation of sort plates and all downstream pipetting steps
538 were performed on a Biomek i7 Automated Workstation (Beckman Coulter). After addition of 1 µL
539 0.2% SDS, samples were incubated at 55 °C for 7 min with shaking (500 rpm). We added 1 µL
540 12.5% Triton-X to each well to quench the SDS and 12.5 µL NEBNext High-Fidelity 2× PCR
541 Master Mix (NEB). Samples were PCR-amplified (72 °C 5 min, 98 °C 30 s, (98 °C 10 s, 63 °C 30 s,
542 72 °C 60 s) × 12 cycles, held at 12 °C). After PCR, all wells were combined. Libraries were purified
543 according to the MinElute PCR Purification Kit manual (Qiagen) using a vacuum manifold (QIAvac
544 24 plus, Qiagen) and size selection was performed with SPRI Beads (Beckmann Coulter, 0.55x
545 and 1.5x). Libraries were purified one more time with SPRI Beads (Beckmann Coulter, 1.5x).
546 Libraries were quantified using a Qubit fluorimeter (Life technologies) and the nucleosomal
547 pattern was verified using a Tapestation (High Sensitivity D1000, Agilent). The library was
548 sequenced on a HiSeq2500 sequencer (Illumina) using custom sequencing primers, 25% spike-
549 in library and following read lengths: 50 + 43 + 40 + 50 (Read1 + Index1 + Index2 + Read2).
550

551 **Raw data processing and quality control**

552 For each read, we first appended the cell barcode metadata to the read name. The cell barcode
553 consisted of four pieces (P7, I7, I5, P5) which were derived from the index read files. We first
554 corrected for sequencing errors by calculating the Levenshtein distance between each of the four
555 pieces and a whitelist of possible sequences. If the piece did not perfectly match a whitelisted
556 sequence, we took the best matching sequence if it was within 2 edits and the next matching
557 sequence was at least 2 additional edits away. If none of these conditions were met, we discarded
558 the read from further analyses.

559 We trimmed Nextera adapter sequences from sequence reads using trim_galore (v.0.4.4,
560 https://github.com/FelixKrueger/TrimGalore) with default parameters. We used bwa mem[97]
561 (v.0.7.17-r1188) to align reads to the hg19 reference genome with the options '-M -C'. We then
562 used samtools[98] to filter out reads that did not align to the autosomes or sex chromosomes and

bioRxiv preprint doi: https://doi.org/10.1101/693671; this version posted July 9, 2019. The copyright holder for this preprint (which was not certified by peer review) is the author/funder, who has granted bioRxiv a license to display the preprint in perpetuity. It is made available under aCC-BY-NC-ND 4.0 International license.

563 low mapping quality reads (MAPQ<30). We used samtools fixmate (v.1.6) to perform additional
564 checks for FR proper pairs and removed secondary or unmapped reads. We used the
565 MarkDuplicates tool from picard (https://broadinstitute.github.io/picard/) to remove duplicates on
566 a per-barcode basis with 'BARCODE_TAG' option. For each experiment, we used a Gaussian
567 mixture model on log-transformed read depths to separate barcodes with a 99% probability of
568 belonging to the high read distribution, likely representing real cells, from those in the low read
569 distribution, likely representing background reads. We then set an additional threshold of 1000
570 read depth, reasoning that low read cells would contribute additional noise to clustering.

571

572 **Cluster analysis for snATAC-seq**

573 We split the genome into 5 kb windows and removed windows overlapping blacklisted regions
574 from ENCODE (https://sites.google.com/site/anshulkundaje/projects/blacklists). For each
575 experiment, we then created a sparse *m* x *n* matrix containing read depth for *m* cells passing read
576 depth thresholds at *n* windows. For further quality checks, we performed initial clustering for each
577 experiment individually using scanpy[99] (v.1.4). We extracted highly variable windows using mean
578 read depths and normalized dispersion. After normalization to a uniform read depth and log-
579 transformation of read depth, we regressed out the log-transformed total read depth for each cell.
580 We then performed PCA and extracted the top 50 principal components. We used these
581 components to calculate the nearest 30 neighbors using the cosine metric, which were
582 subsequently used for UMAP dimensionality reduction with the parameters 'min_dist=0.3' and
583 Louvain clustering with the parameters 'resolution=1.5'. For each experiment, we removed 2,709
584 cells that were in clusters corresponding to low read depth.

585 After removing these cells, we used similar methods to cluster cells from all experiments together
586 with the following modifications. We extracted highly variable windows across cells from all
587 experiments. Since read depth was a technical covariate specific to each experiment, we
588 regressed this out on a per-experiment basis. We used mutual nearest neighbors correction[30]
589 (mnnpy, v.0.1.9.4) to adjust for batch effects across experiments with the parameters 'k=10'. We
590 then performed clustering as described above. We used chromatin accessibility at windows
591 overlapping promoters for marker hormones (*GCG*, *INS-IGF2*, *SST*, and *PPY*) to assign cell types
592 for the endocrine islet cell types (alpha, beta, delta, and gamma). We performed re-clustering on
593 non-endocrine islet clusters and used chromatin accessibility at windows around marker genes
594 from single cell RNA-seq to assign cluster labels. In our clustering results, we identified a cluster
595 of 694 alpha cells that were mostly derived from a single donor (96% of cells from Islet 1). Because

bioRxiv preprint doi: https://doi.org/10.1101/693671; this version posted July 9, 2019. The copyright holder for this preprint (which was not certified by peer review) is the author/funder, who has granted bioRxiv a license to display the preprint in perpetuity. It is made available under aCC-BY-NC-ND 4.0 International license.

596 we were uncertain whether this represented technical or biological differences, we excluded this
597 cluster from further analyses. We also excluded a cluster of 192 cells likely representing lower
598 quality cells as it had low intra-cluster similarity and lower fraction of reads in peaks.

599

600 **Comparison to bulk and sorted islet ATAC-seq**

601 We obtained raw sequence data of ATAC-seq for 42 bulk islet samples from four prior
602 studies[14,27,28,72] and 4 bulk pancreas samples from ENCODE. We re-processed all samples with
603 a uniform pipeline: we aligned all reads to hg19 with bwa mem, identified and removed duplicate
604 reads with picard MarkDuplicates, and called peaks with MACS2 (v.2.1.2) with the parameters
605 '—shift -100 –extsize 200 –keep-dup all'. For the three islet snATAC-seq samples, we used
606 aggregated per-barcode deduplicated reads to call peaks. We defined all possible accessibility
607 peaks by filtering out ENCODE blacklisted regions and retaining merged peaks on autosomal
608 chromosomes found in more than one sample. We then calculated the read coverage at all
609 possible accessibility peaks and TPM-normalized the counts. We calculated the Spearman
610 correlation between normalized read coverages and used hierarchical clustering to assess
611 similarity between bulk islet samples. To check peak call overlap between aggregated single cell
612 ATAC and bulk ATAC data, we split peaks based into promoter proximal (+/-500 bp from
613 GENCODE transcript TSS) and distal peaks based on promoter overlap. For each cluster, we
614 calculated the percentage of aggregate peaks that overlapped merged autosomal bulk peaks and
615 individual sample-level autosomal bulk peaks.

616 We also obtained raw sequence data of ATAC-seq from flow-sorted pancreatic cells (alpha, beta,
617 acinar, ductal) from two prior studies[35,36] and re-processed all samples with the uniform pipeline
618 described above. For alpha, beta, and exocrine cells from islet snATAC-seq, we split reads on a
619 per-donor and per-cluster basis to obtain read files. Because total read depth was highly variable
620 across sorted samples, we merged autosomal peaks after filtering out ENCODE blacklist regions.
621 We calculated read coverage in each sample for each merged peak and TPM normalized count
622 values. We then calculated the Spearman correlation between normalized read coverages and
623 used hierarchical clustering to assess similarity between sorted and snATAC-seq islet samples.

624

625 **Identifying marker peaks of chromatin accessibility**

626 To identify peaks for each cell type, we aggregated reads for all cells within a cluster or sub-
627 cluster. We shifted reads aligning to the positive strand by +4 bp and reads aligning to the negative

bioRxiv preprint doi: https://doi.org/10.1101/693671; this version posted July 9, 2019. The copyright holder for this preprint (which was not certified by peer review) is the author/funder, who has granted bioRxiv a license to display the preprint in perpetuity. It is made available under aCC-BY-NC-ND 4.0 International license.

628 strand by -5 bp, extended reads to 200 bp, and centered reads. We used MACS2[100] to call peaks
629 of chromatin accessibility for each aggregated read file with the following settings '--nomodel --
630 keep-dup all'. We removed peaks that overlapped ENCODE blacklisted regions[101]. We then used
631 bedtools[102] to merge peaks from all clusters and sub-clusters to create a superset of islet
632 regulatory peaks.

633 We generated a sparse *m* x *n* binary matrix containing binary overlap between *m* peaks in the
634 superset of islet regulatory peaks and *n* cells. We then calculated t-statistics of peak specificity
635 for each cluster or sub-cluster through linear regression models. We used binary encodings to
636 specify which donor a given cell came from as covariates in the model. For each peak and cluster,
637 we used binary encoding of read overlap with the peak as the predictor and whether a cell was in
638 the cluster (1 if yes, -1 if no) as the outcome.

639

640 **Matching islet snATAC-seq with scRNA-seq clusters**

641 To verify that clusters definitions and labels from single cell chromatin accessibility data matched
642 those from single cell expression data, we obtained published single cell RNA-seq data from 12
643 non-diabetic islet donors[23]. Because cluster definitions for all cell types were not available, we re-
644 analyzed the data and performed clustering analyses. Starting with the gene expression matrix,
645 we first performed quality control steps to remove potential doublets. For each marker gene of
646 different cell types *GCG* (alpha), *INS* (beta), *SST* (delta), *PPY* (gamma), *CTRB2* (acinar), *CFTR*
647 (ductal), *PLVAP* (endothelial), *PDGFRB* (stellate), and *C1QC* (immune) we used a Gaussian
648 mixture model on log-transformed read depth to determine whether a cell expressed the gene
649 (high distribution) or not (low distribution). We verified that cells expressing more than one marker
650 gene had on average higher read depth and expressed more genes (Supplementary Figure 3a,b).
651 We regressed out covariates including sex, BMI, and read depth, and separated cells by donor of
652 origin. We then used MNN correction[30] to adjust for batch effects. After scaling the data, we
653 performed PCA and used the top 50 principal components to calculate the 10 nearest neighbors
654 using the cosine metric. We used the nearest neighbor map for UMAP dimensionality reduction
655 with the parameters 'min_dist=0.3' and to perform Louvain clustering with the parameters
656 'resolution=1' (Supplementary Figure 3c). We used a similar regression framework as the
657 chromatin accessibility marker peaks to calculate t-statistics for gene specificity for each cluster
658 (Supplementary Figure 3d,e) with the following modifications: we included sex, BMI, and log-
659 transformed read coverage as covariates and used $\log_2$ read counts for each gene instead of
660 binary peak coverage as the predictor.

bioRxiv preprint doi: https://doi.org/10.1101/693671; this version posted July 9, 2019. The copyright holder for this preprint (which was not certified by peer review) is the author/funder, who has granted bioRxiv a license to display the preprint in perpetuity. It is made available under aCC-BY-NC-ND 4.0 International license.

661

662 We used the Spearman correlation between t-statistics from islet snATAC-seq and scRNA-seq
663 data to match up clusters. Specifically, we took the top 100 (sorted by descending t-statistic) most
664 specific promoter peaks for each cluster or sub-cluster to define a list of genes for comparison.
665 To facilitate one-to-one comparisons between the two datasets, for this analysis only we defined
666 promoter peaks as peaks within +/-500 bp of a GENCODE v19 gene TSS. This list contained 966
667 genes, which is less than 100x13 (number of clusters) because 1) marker genes were sometimes
668 shared between sub-clusters and 2) not all genes were present in the expression dataset. For
669 each cluster from accessible chromatin data, we then compared t-statistics of genes in the list
670 with t-statistics for all clusters from single cell expression using the Spearman correlation, which
671 is robust to very specific marker genes such as insulin which could otherwise bias these
672 comparisons.

673

674 **Motif enrichment with chromVAR**

675 We used chromVAR[37] (v.1.5.0) to calculate TF motif-associated difference between cell
676 populations. We first calculated counts per peak per cell matrix and then input it to chromVAR.
677 We filtered cells with minimal reads less than 1500 (min_depth=1500) and peaks with fraction of
678 reads less than 0.15 (min_in_peaks=0.15) by using 'filterSamplesPlot' function from chromVAR.
679 We also corrected GC bias based on 'BSgenome.Hsapiens.UCSC.hg19' using 'addGCBias'
680 function. Then we used the Jaspar motifs from 'getJasparMotifs' function with default parameter
681 and calculated the deviation z-scores for each TF motif in each cell by using 'computeDeviations'
682 function. High-variance TF motifs across all cell types were selected by 'computeVariability'
683 function using cut-off 1.2 (N=111). For each of these variable motifs, we calculated the mean z-
684 score for each cell types and normalized the values to 0 (minimal) and 1 (maximal).

685

686 **Comparison of alpha and beta cell states**

687 To identify TF motifs variable between alpha or beta cell states, we performed two-sided Student's
688 T-test on motif z-scores between cells labeled as alpha 1 (GCG^{high}) and alpha 2 (GCG^{low}) cells or
689 beta 1 (INS^{high}) and beta 2 (INS^{low}). We adjusted raw p-values with the Benjamini-Hochberg
690 procedure to obtain FDR. Motifs with FDR less than 0.05 and absolute difference (Δ) in z-score
691 (between GCG^{high}/GCG^{low} alpha or INS^{high}/INS^{low} beta) greater than 0.5 were defined as differential
692 motifs (N=46 for beta cells, N=109 for alpha cells and N=111 motifs combined). For these 111

bioRxiv preprint doi: https://doi.org/10.1101/693671; this version posted July 9, 2019. The copyright holder for this preprint (which was not certified by peer review) is the author/funder, who has granted bioRxiv a license to display the preprint in perpetuity. It is made available under aCC-BY-NC-ND 4.0 International license.

693 motifs that were variable between alpha or beta cell states, we summarized the mean z-scores
694 over GCG^{high}, GCG^{low}, INS^{high} and INS^{low} cells and plotted the normalized value. In order to check
695 how motif usage changed along the trajectories, we smoothed motif z-scores along the trajectory
696 for alpha and beta cells separately at step=0.05, using the shrinkage version of cubic regression
697 spline ('gam' function from the R package 'mgcv' (v1.8.28) with parameter bs='cs'). We then
698 smoothed motif enrichment profiles and normalized values for visualization. We identified specific
699 TFs likely driving enrichments for a given motif through high Spearman correlation (σ>.9) between
700 motif enrichment and promoter accessibility across the trajectory.

701 To analyze differential promoter accessibility between alpha and beta cell states, we first
702 calculated the binary promoter by cell matrix containing information about read overlap per cell in
703 a promoter peak. Based on this matrix and cell cluster labels, we performed two-sided Fisher's
704 exact tests between hormone-high and hormone-low states of alpha, beta, and delta cells for
705 each promoter against the null hypothesis that the promoter had similar accessibility across
706 states. We used Bonferroni adjusted p-values (adjusted p-value<0.01) for alpha and beta cells
707 with the sign of the $\log_2$ transformed odds ratio to identify genes whose promoter had either
708 increased or decreased accessibility across states. Differentially-accessible promoters were
709 further input into Enrichr[103] (v.1.0) to perform GO term enrichment analysis on biological
710 processes terms (2018 version). To identify more specific processes, we filtered for gene ontology
711 terms that contained less than 150 total genes.

712 To plot the profile of each promoter across pseudo-state, we first binned alpha cells or beta cells
713 to 100 bins along the state trajectory. For each bin, we calculated the fraction of cells had a peak
714 in the promoter region for each promoter. Then we smoothed these 100 fractions using the 'loess'
715 function from R. The smoothed data were then normalized and clustered using k-medoids
716 clustering, with k determined by optimum average silhouette width using the 'pamk' function from
717 the R 'fpc' package (v.2.1.11.1). Genes attributed to the promoters in each cluster were then used
718 to perform GO term enrichment analysis.

719 In order to compare with previous published data, we collected gene lists from Xin et al.[23]. We
720 obtained four gene lists for Beta 1-4 subpopulations (Supplementary Table S3 in Xin et al.). For
721 each gene list, we performed gene set enrichment analysis[104] using significantly differential
722 promoters (from Figure 2a) as the gene lists to assess whether alpha and beta cell states showed
723 concordant differences (i.e. differential promoters for GCG^{low} and GCG^{high} alpha to compare beta
724 cell states and vice versa for alpha cells).

bioRxiv preprint doi: https://doi.org/10.1101/693671; this version posted July 9, 2019. The copyright holder for this preprint (which was not certified by peer review) is the author/funder, who has granted bioRxiv a license to display the preprint in perpetuity. It is made available under aCC-BY-NC-ND 4.0 International license.

725

726 **Ordering alpha and beta cells along a trajectory and finding dynamic peaks**

727 We used Cicero[6] (v.1.1.5) to order all alpha and beta cells along separate trajectories. We started
728 with a sparse binary matrix encoding overlap between the superset of islet regulatory peaks and
729 cells. We extracted all cells belonging to alpha cell sub-clusters and filtered out peaks that were
730 not present in alpha cells. We used the aggregate_nearby_peaks function from Cicero to find
731 peaks within 10 kb and merging their counts to make an aggregate matrix. We then chose peaks
732 to define progress with the aggregated matrix by using the differentialGeneTest function from
733 monocle2[47] to search for peaks that were differentially accessible between the GCG^{high} and
734 GCG^{low} states (FDR<.1), while modeling total peaks in each cell as a covariate. We then used
735 DDRTree to reduce dimensions and ordered cells along the trajectory, setting the root position as
736 the state with the highest glucagon promoter accessibility. We grouped cells into 10 bins based
737 on their trajectory values. Then we repeated the same procedure for beta cells, with the
738 modification of setting the root position by insulin promoter accessibility.

739

740 **GWAS enrichment with aggregate peak annotations**

741 We used cell type specific (CTS) LD score regression[69,105] (v.1.0.0) to calculate enrichment for
742 GWAS traits. We obtained GWAS summary statistics for quantitative traits related to diabetes[13,55–
743 59], diabetes[10], and control traits including psychiatric and autoimmune diseases[60–67]. We prepared
744 summary statistics to the standard format for LD score regression. We used peaks from
745 aggregated reads for each cluster as a binary annotation, and the superset of islet regulatory
746 peaks as the background control. For each trait, we then used CTS LD score regression to
747 estimate the enrichment coefficient of each annotation jointly with the background control.

748

749 **GWAS enrichment with single cell annotations**

750 We determined genetic enrichment of accessible chromatin profiles in individual cells. We first
751 split the genome into 5 kb windows and removed windows overlapping blacklisted regions from
752 ENCODE. We created a sparse m x n matrix containing read depth for m cells passing read depth
753 thresholds at n windows, and extracted highly variable (HV) windows using mean read depths
754 and normalized dispersion. We then retained genetic variants mapping in HV windows with minor
755 allele frequency [MAF]>.05 mapping outside of the major histocompatibility complex region (MHC,
756 defined by chr6:25,000,000-35,000,000 in hg19 coordinates).

bioRxiv preprint doi: https://doi.org/10.1101/693671; this version posted July 9, 2019. The copyright holder for this preprint (which was not certified by peer review) is the author/funder, who has granted bioRxiv a license to display the preprint in perpetuity. It is made available under aCC-BY-NC-ND 4.0 International license.

757 As the accessible chromatin profiles from an individual cell are sparse, we used the bagging
758 algorithm in the make_cicero_cds function from Cicero[6] to aggregate cells into groups of 10. For
759 each aggregate cell group, we created a binary annotation based on mapped reads for cells in
760 the aggregate. We also created baseline annotations consisting of pooled islet cell type
761 accessible chromatin sites and the 53 baseline v1.1 annotations from LD score regression[68]. We
762 then annotated all variants in HV windows with the aggregate cell and baseline annotations. We
763 determined enrichment of HV variant annotations for fasting glucose level[56], type 2 diabetes[10],
764 and two control traits, major depressive disorder[66] and lupus[63] GWAS data. In order to correct for
765 the confounding effects of linkage disequilibrium (LD), we performed LD pruning of GWAS data
766 for each trait by first sorting variants based on p-value and iteratively removing variants in LD
767 (r^2>.5, 1000 Genomes European subset) with a more significant variant. To then perform
768 enrichment tests on pruned GWAS data we used a previously described method polyTest[106] to
769 jointly model the annotation for each aggregated cell group with the baseline pooled site and 53
770 annotations from LD score baseline v1.1. We then calculated a z-score for each aggregate cell
771 based on the effects and standard error from the resulting model. As the grouping method for
772 Cicero uses bootstrap aggregation, a given cell was potentially assigned to multiple aggregates.
773 We therefore calculated an enrichment z-score for each individual cell by averaging enrichment
774 z-scores for each cell across its respective aggregates.

775 To identify TFs correlated with trait enrichments, we calculated the Spearman correlation
776 coefficient between fasting glucose or type 2 diabetes single cell GWAS enrichment z-scores and
777 chromVAR motif enrichment z-scores using data from all cells or within beta cells. Within each
778 trait, we used Bonferroni correction to adjust correlation p-values for multiple tests.

779

780 **Mapping allelic imbalance within clusters**

781 Genomic DNA for genotyping was extracted either from spare islet nuclei (donors 1 and 2), or
782 acinar cells (donor 3). Genomic DNA was extracted using the DNeasy Blood & Tissue Kits
783 (Qiagen) according to manufacturer's protocol for purification of total DNA from animal blood or
784 cells. Extracted genomic DNA was used for genotyping on the Illumina Infinium Omni2.5-8 v1.4
785 genotyping array. For genotypes that passed quality filters (non-missing, MAF>.01 in European
786 or African populations in 1KGP), we then imputed genotypes into the HRC reference panel r1.1[107]
787 using the Michigan Imputation Server[108]. Post-imputation, we removed genotypes with low
788 imputation quality (R^2<.3). As an additional filter to remove potential false positive heterozygote
789 genotype calls, we removed variants that had greater than 20 read coverage without reads for

bioRxiv preprint doi: https://doi.org/10.1101/693671; this version posted July 9, 2019. The copyright holder for this preprint (which was not certified by peer review) is the author/funder, who has granted bioRxiv a license to display the preprint in perpetuity. It is made available under aCC-BY-NC-ND 4.0 International license.

790 both alleles. Using cluster assignments for each cell, we split mapped reads for each donor into
791 cluster-specific reads. For cluster-specific reads, we used the WASP pipeline[109] (v.0.3.0) to
792 correct for reference mapping bias at heterozygous variants. We then used a two-sided binomial
793 test to assess imbalance at heterozygous variants, assuming a null hypothesis where both alleles
794 were equally likely to be observed. For each variant, we then calculated combined imbalance z-
795 scores across donors using Stouffer's z-score method and used sequencing depth to weight
796 statistics from each sample.

797

798 **Predicting genetic variant effects on chromatin accessibility**

799 We used deltaSVM[70] to predict the effects of non-coding variants on chromatin accessibility in
800 each cell type and cell state. We obtained sequences underlying promoter-distal (>+/-500 bp from
801 GENCODEv19 transcript TSS for protein coding and long non-coding RNA genes) peaks for each
802 cluster, used 'genNullSeqs' to generate background sequences, and then trained a model for
803 each cluster with 'gkmtrain' with default settings. For all possible combinations of 11mers, we then
804 used 'gkmpredict' to predict the effects of 11mers based on the trained model for the cluster. For
805 each SNP in the HRC reference panel r1.1[107] overlapping an islet cell type accessible chromatin
806 site, we created 19 bp sequences around each allele (9 bp flanking either side of the variant
807 base). We then used the 'deltasvm.pl' script to calculate deltaSVM scores for differential
808 chromatin accessibility between variant alleles. We built a null distribution by randomly permuting
809 the effects of 11mers and re-calculating deltaSVM scores and using the parameters of this null
810 distribution, we calculated z-scores for each variant. From variant z-scores we calculated p-values
811 and then q-values and considered variants significant at FDR<.1.

812 For variants with predicted effects on chromatin accessibility in alpha or beta cells, we categorized
813 them based on their effects across cell type and states. Variants with significant effects in both
814 alpha cell states but neither beta cell state were classified as "alpha" (n=10,564) and vice versa
815 for "beta" (n=12,833). Variants with significant effects in GCG^{high} alpha and INS^{high} beta states but
816 not GCG^{low} alpha and INS^{low} beta states were classified as "hormone-high" (n=15,769), and vice
817 versa for "hormone-low" (n=12,471). Variants with significant effects in all four alpha and beta cell
818 states were classified as "shared" (n=31,331). We also determined the concordance in the
819 direction of effect for variants across alpha and beta cell states. For the set of variants with
820 significant effects in each state, we calculated the fraction of variants where the allele with the
821 higher predicted effect had a higher predicted effect in other states. We determined significance
822 using a two-sided binomial test assuming an expected fraction of 50%. We assessed enrichment

bioRxiv preprint doi: https://doi.org/10.1101/693671; this version posted July 9, 2019. The copyright holder for this preprint (which was not certified by peer review) is the author/funder, who has granted bioRxiv a license to display the preprint in perpetuity. It is made available under aCC-BY-NC-ND 4.0 International license.

823 of predicted effect variants in alpha or beta cell states for islet caQTLs[72] compared to any islet
824 caQTL in alpha or beta cell sites using two-sided Fisher's exact tests. We then stratified variants
825 with predicted effects by category (hormone-high, hormone-low, alpha, or beta) and assessed
826 enrichment of caQTLs with predicted effects within each category with two-sided Fisher's exact
827 tests.

828

829 **Luciferase gene reporter assays**

830 We selected fine-mapped T2D risk variants with deltaSVM predictions (rs7482891, rs34584161,
831 rs17712208, rs78840640, rs4679370) to test for allelic differences in enhancer activity in MIN6
832 beta cells using luciferase reporter assays. We cloned sequences containing reference alleles in
833 the forward orientation upstream of the minimal promoter of firefly luciferase vector pGL4.23
834 (Promega) using KpnI and SacI restriction sites. For rs7482891 (*TH*) and rs34584161 (*RNF6*),
835 we cloned alternative alleles in the forward direction in the same manner as the reference alleles.
836 For rs17712208 (*PROX-AS1*), rs78840640 (*IGF2BP3*), and rs4679370 (*SLC12A8*), we
837 introduced the alternative alleles via site-directed mutagenesis (SDM) using the NEB Q5 Site-
838 Directed Mutagenesis kit (New England Biolabs). We designed primers using NEBaseChanger
839 (v.1.2.8), and we used 10ng of the reporter plasmid containing the reference allele as a template
840 in site-directed mutagenesis using Q5 Hot Start High-Fidelity master mix (New England Biolabs).
841 4uL of the SMD PCR product was treated with KLD mix (New England Biolabs) and transformed
842 into DH5a *E. coli*. We miniprepped plasmids using the Qiaprep Spin Mini kit (Qiagen) and verified
843 plasmid sequences through Sanger sequencing with the RV3 primer.

844

845 SDM primers:

846

847 rs17712208 (*PROX-AS1*)
848 SDM primer (left): GGAGCTATGGaTAATTATTGACTG
849 SDM primer (right): ATTAACGATCCAGTCAGC

850

851 rs78840640 (*IGF2BP3*)
852 SDM primer (left): ATCAGATTTGgTGAGAAAGAAGAAC
853 SDM primer (right): GCCCATCAATTCTGAGCATG

854

855 rs4679370 (*SLC12A8*)

bioRxiv preprint doi: https://doi.org/10.1101/693671; this version posted July 9, 2019. The copyright holder for this preprint (which was not certified by peer review) is the author/funder, who has granted bioRxiv a license to display the preprint in perpetuity. It is made available under aCC-BY-NC-ND 4.0 International license.

856 SDM primer (left): ATCAGTAAGCcCCTAAAGCCTG
857 SDM primer (right): TAACTTGAGGCAATGGTG
858

859 Construct primers:
860

861 rs7482891 (*TH*)
862 construct primer (left): AGAGGTCTGAGGAGCCCTTG
863 construct primer (right): TAGACCCTGCAGAGCCACAG
864

865 rs34584161 (*RNF6*)
866 construct primer (left): AAGCTGACAGACAGAGGGTCA
867 construct primer (right): GGGCTTCATAAACATCAGCA
868

869 rs17712208 (*PROX-AS1*)
870 construct primer (left): AAGCCCACCTTCGTAAACAT
871 construct primer (right): TGAAGTAGCTCCCAGTGAAGG
872

873 rs78840640 (*IGF2BP3*)
874 construct primer (left): CACAATGAAGCCATGTCCTTT
875 construct primer (right): TCAGCTTTCTATTTTGGGGAAA
876

877 rs4679370 (*SLC12A8*)
878 construct primer (left): TCAATGTCTACCTCAAAATTCTTTGT
879 construct primer (right): CACTGCAGCCTTAAACTCCTG
880

881 We seeded MIN6 cells into 6 (or 12)-well trays at 1 million cells per well. At 80% confluency, we
882 co-transfected cells with 500ng of the experimental firefly luciferase vector pGL4.23 containing
883 the alternative allele, reference allele, or an empty vector and 50ng of the vector pRL-SV40
884 (Promega) using the Lipofectamine 3000 reagent (Thermo Fisher). We performed all transfections
885 were performed in triplicate. Six hours after transfection, we replaced MIN6 growth media
886 consisting of modified DMEM containing 1.5g/L sodium bicarbonate supplemented with 4% heat
887 inactivated FBS, gentamicin, and 50uM beta-mercaptoethanol. We lysed cells 48 hours after

bioRxiv preprint doi: https://doi.org/10.1101/693671; this version posted July 9, 2019. The copyright holder for this preprint (which was not certified by peer review) is the author/funder, who has granted bioRxiv a license to display the preprint in perpetuity. It is made available under aCC-BY-NC-ND 4.0 International license.

888 transfection and assayed for Firefly and Renilla luciferase activities using the Dual-Luciferase
889 Reporter system (Promega). We normalized Firefly activity to Renilla activity and compared it to
890 the empty vector, and normalized results were expressed as fold change compared to empty
891 vector control per allele. We used a two-sided Student's T-test to compare the luciferase activity
892 between the two alleles.
893

894 **TF motif enrichment within predicted effect variant categories**
895 For each cell- or state-resolved category (hormone-high, hormone-low, alpha, beta) of variants
896 with predicted effects, we extracted 29 bp sequences (+/-14 bp around each SNP) corresponding
897 to the higher or lower predicted effect allele. Here, we reasoned that extracting sequences for a
898 larger window around SNPs would alleviate bias for the analysis against motifs with longer PWMs.
899 We then used AME from the MEME suite[110] (v.4.12.0) to predict motif enrichment, using position
900 weight matrices from the latest non-redundant motif library JASPAR 2018[38]. We used sequences
901 from the higher effect allele as the test set and sequences from the lower effect allele as the
902 background set. Because motif for TFs within the same structural family can potentially show
903 similar enrichment, we used the TFClass database (http://tfclass.bioinf.med.uni-goettingen.de/)
904 to group motifs by TF family. To determine which TF was most likely driving the enrichment, we
905 used min-max normalized promoter accessibility within TF family members with a promoter peak
906 in alpha or beta cells and highlighted corresponding cell type patterns of promoter accessibility.

907

908 **Enrichment of predicted variants for lower frequency variants**
909 We obtained genome-wide summary statistics of T2D from the DIAMANTE consortium[10]. We
910 estimated LD patterns for variants with MAF<.05 using HRC imputed genotype data from samples
911 in the UK Biobank (UKB, March 2018 release). We randomly selected 10,000 non-related UKB
912 samples of European ancestry and calculated LD between lower frequency variants using PLINK
913 (v.1.90b6.7). We then LD-pruned variants with MAF<.05 in DIAMANTE T2D data by first sorting
914 variants based on their p-values and then removed variants in r^2>.5 with a more significant variant.
915 Using the LD-pruned results, we then determined enrichment of variants with predicted effects on
916 endocrine cell types. We created sets of variants that had significant effects (FDR<.1) in any
917 endocrine cell type, as well as variants with FDR<.1 for each cell type. For alpha, beta and delta
918 cells, we considered variants with effects in either cell state. We then created a background set
919 of variants as those without significant effects in any endocrine cell type (all FDR>.1). We set a
920 series of p-value thresholds ($5x10^{-8}$, $1x10^{-7}$, $1x10^{-6}$, $1x10^{-5}$, $1x10^{-4}$, $1x10^{-3}$), and at each threshold

bioRxiv preprint doi: https://doi.org/10.1101/693671; this version posted July 9, 2019. The copyright holder for this preprint (which was not certified by peer review) is the author/funder, who has granted bioRxiv a license to display the preprint in perpetuity. It is made available under aCC-BY-NC-ND 4.0 International license.

921 determined the fraction of variants in each category as well as background variants reaching that
922 p-value threshold to calculate a fold-enrichment based on these fractions compared to
923 background. We determined significance of the enrichments by using a two-sided binomial test
924 of the counts for each category using the background fraction as the expected count.

925

926 **Chromatin co-accessibility with Cicero**

927 We used Cicero[6] to calculate peak-peak co-accessibility scores for alpha and beta cells. Like the
928 trajectory analysis, we started with a sparse binary matrix encoding overlap between the superset
929 of islet regulatory peaks and cells. We extracted all cells belonging to alpha cell sub-clusters and
930 filtered out peaks that were not present in alpha cells. We then used the make_cicero_cds function
931 to aggregate cells based on the 50 nearest neighbors from the UMAP reduced dimensions. We
932 then used Cicero to calculate co-accessibility scores using a window size of 1 Mb and a distance
933 constraint of 500 kb, leaving other parameters at the default setting. We then repeated the same
934 procedure for beta cells. We used two-sided Fisher's exact tests to assess whether distal co-
935 accessible sites had higher accessibility in either hormone-high or -low states, and defined
936 significance at FDR<.1. To compare promoter-distal co-accessibility links that had higher
937 accessibility in the same direction (either both hormone-high or hormone-low), we used differential
938 promoters between states (from the previous analysis in Figure 2).

939

940 **Enrichment of islet Hi-C and pcHi-C loops in co-accessible peaks**

941 We obtained sets of merged Hi-C loops[27] and high-confidence promoter capture Hi-C (pcHi-C)
942 loops[76] from public datasets. For Hi-C loops, we used anchors directly from the loops. For pcHi-
943 C loops, we used a 5 kb window centered on the interaction point as the anchor. To compare
944 alpha and beta cell co-accessibility with Hi-C, we then used direct overlap of alpha or beta cell
945 peaks with anchors. For different binned thresholds of co-accessibility in .05 increments, we then
946 calculated distance-matched odds ratios for co-accessible peaks containing Hi-C loops versus
947 non-co-accessible peaks (co-accessibility<0). We then used two-sided Fisher's exact tests to
948 assess significance. We repeated the procedure for high confidence pcHi-C loops for both cell
949 types.

950

bioRxiv preprint doi: https://doi.org/10.1101/693671; this version posted July 9, 2019. The copyright holder for this preprint (which was not certified by peer review) is the author/funder, who has granted bioRxiv a license to display the preprint in perpetuity. It is made available under aCC-BY-NC-ND 4.0 International license.

951 **Annotating fine-mapped diabetes risk variants**

952 We annotated risk signals in compiled fine-mapping data for type 2 diabetes from the DIAMANTE
953 consortium and Biobank Japan studies. For the Biobank Japan T2D GWAS, we constructed LD-
954 based 99% genetic credible sets for main signals at 22 novel loci that were distinct from the
955 DIAMANTE study. We used the East Asian subset of the 1000 Genomes Project to define credible
956 set variants by taking all variants in at least low LD (r^2>.1) with the index variant in a 5 Mb window.
957 We used effect size and standard error estimates to calculate Bayes factors for each variant. For
958 each signal, we then calculated the posterior probability causal probability (PPA) that each variant
959 drives the association by dividing its Bayes factor by the sum of Bayes factors for all variants in
960 the signal's credible set. We then sorted each signal by descending PPA and retained variants
961 that added up to a cumulative probability of .99 to derive 99% credible sets.

962 For each signal, we identified candidate casual variants that were both in the 99% credible set
963 and had a posterior causal probability greater than .01. We intersected these candidate variants
964 with accessible chromatin sites for each islet cell type and cell state, and then identified variants
965 with predicted effects on the overlapping cell types/states. We finally annotated variants based
966 on overlap with sites co-accessible to gene promoters. For target genes linked to diabetes risk
967 variants we determined enriched gene sets using GSEA.

968

969 **Analysis of *INS* promoter 4C data**

970 We downloaded and re-analyzed published 4C data of the *INS* promoter for the beta cell line
971 EndoC-βH1[77] with 4C-ker[111]. We first created a reduced genome using 25 bp flanking sequences
972 of BglII cutting sites. For each of the 3 replicates, we then aligned reads to this reduced genome
973 using bowtie2[112] (v.2.2.9) with the parameter "-N 0 -5 20". We then extracted counts for each
974 fragment from the SAM file after removing self-ligated and undigested fragments, and we used
975 the bedGraph files as input to the R.4Cker package. We generated normalized counts and called
976 high interaction regions using the 'nearBaitAnalysis' function with the parameter 'k=10'.

977

978 **CRISPR/Cas9-mediated enhancer deletion**

979 H1 hESCs (WA01; purchased from WiCell; NIH registration number: 0043) were seeded onto
980 Matrigel®-coated six-well plates at a density of 50,000 cells/cm^2 and maintained in mTeSR1
981 media (StemCell Technologies) for 3-4 days with media changed daily. hESC research was

bioRxiv preprint doi: https://doi.org/10.1101/693671; this version posted July 9, 2019. The copyright holder for this preprint (which was not certified by peer review) is the author/funder, who has granted bioRxiv a license to display the preprint in perpetuity. It is made available under aCC-BY-NC-ND 4.0 International license.

982 approved by the University of California, San Diego, Institutional Review Board and Embryonic
983 Stem Cell Research Oversight Committee.

984 To generate clonal homozygous *KCNQ1* enhancer deletion hESC lines, two sgRNAs targeting
985 the enhancer were designed and cloned into Px333-GFP, a modified version of Px333 (#64073,
986 Addgene). The plasmid was transfected into H1 hESCs with XtremeGene 9 (Roche). 24 hours
987 later, 5000 GFP^+ cells were sorted into a well of six-well plate. Individual colonies that emerged
988 within 5-7 days after transfection were subsequently transferred manually into 48-well plates for
989 expansion, genomic DNA extraction, PCR genotyping, and Sanger sequencing. sgRNA oligos
990 and genotyping primers are listed below. For control clones, we transfected the Px333-GFP
991 plasmid into H1 hESCs and subjected the cells to the same workflow as H1 hESCs transfected
992 with sgRNAs.

993 sgRNA oligos:

994 KCNQ1_sgRNA1-s: ACTGTCGGGCCCATCTGCCA
995 KCNQ1_sgRNA1-as: TGGTTGGATCTGTTGCGGGG

996 Genotyping primers:

997 Span-F: AGTGGGGCCATGAACAATAA
998 Span-R: GCCTGAGTTTCCGTGACTGT

999

1000 **Pancreatic differentiation of enhancer-deleted hESCs clones**
1001 hESCs were differentiated in a suspension-based format using rotational culture with some
1002 modifications to a published protocol[83]. Undifferentiated hESCs were aggregated by preparing a
1003 single cell suspension in mTeSR media (STEMCELL Technologies) at $1x10^6$ cells/mL and
1004 overnight culture in six-well ultra-low attachment plates (Costar) with 5.5ml per well on an orbital
1005 rotator (Innova2000, New Brunswick Scientific) at 100 rpm. The following day, undifferentiated
1006 aggregates were washed in DMEM/F12 (VWR) and differentiated using a multistep protocol with
1007 daily media changes and continued orbital rotation at either 100 rpm or at 108 rpm from days 8
1008 to 28. In addition to 1% GlutaMAX™ (Gibco) and 15 mM (days 0-10) or 20 mM (days 11-28)
1009 glucose, MCDB 131 media (Life Technologies) was supplemented with 0.5% (days 0-5) or 2%
1010 (days 6-14) fatty acid-free BSA (Proliant), 1.5 g/L (days 0-5 and days 11-28) or 2.5 g/L (days 6-
1011 10) $NaHCO_3$ (Sigma-Aldrich), and 0.25 mM (days 3-10) ascorbic acid (Sigma-Aldrich).

bioRxiv preprint doi: https://doi.org/10.1101/693671; this version posted July 9, 2019. The copyright holder for this preprint (which was not certified by peer review) is the author/funder, who has granted bioRxiv a license to display the preprint in perpetuity. It is made available under aCC-BY-NC-ND 4.0 International license.

1012 Human Activin A, mouse Wnt3a, and human KGF were purchased from R&D Systems. Other
1013 media components included ascorbic acid (Sigma-Aldrich), Insulin-Transferrin-Selenium-
1014 Ethanolamine (ITS-X; Thermo Fisher Scientific), $ZnSO_4$ (Sigma-Aldrich), heparin (Sigma-Aldrich),
1015 retinoic acid (RA) (Sigma-Aldrich), SANT-1 (Sigma-Aldrich), 3,3′,5-Triiodo-L-thyronine (T3)
1016 (Sigma-Aldrich), the protein kinase C activator TPB (EMD Chemicals), the BMP type 1 receptor
1017 inhibitor LDN-193189 (Stemgent), the TGFβ type 1 activin like kinase receptor ALK5 inhibitor,
1018 ALK5 inhibitor II (Enzo Life Sciences), N-Acetyl-L-cysteine (Sigma), R428 (SelleckChem), Trolox
1019 (EMD Millipore), γ-secretase inhibitor XX (Calbiochem).

1020

1021 Day 0: MCDB 131, 100ng/mL Activin, 25ng/mL mouse Wnt3a

1022 Day 1 – Day 2: MCDB 131, 100ng/mL Activin A

1023 Day 3 – Day 5: MCDB 131, 50ng/mL KGF

1024 Day 6 – Day 7: MCDB 131, 50ng/mL KGF, 0.25 μM SANT-1, 1 μM RA 100 nM LDN-193189, 200
1025 nM TPB, 0.5% ITS-X

1026 Day 8 – Day 10: MCDB 131, 2ng/mL KGF, 0.25 μM SANT-1, 0.1 μM RA, 200 nM LDN-193189,
1027 100 nM TPB, 0.5% ITS-X

1028 Day 11 – Day 13: MCDB 131, 0.25 μM SANT-1, 0.05 μM RA, 100 nM LDN-193189, 1 μM T3, 10
1029 μM ALK5i II, 10 μM $ZnSO_4$, 10 μg/mL heparin, 0.5% ITS-X

1030 Day 14 – Day 21: MCDB 131, 100 nM LDN-193189, 1 μM T3, 10 μM ALK5i II, 10 μM $ZnSO_4$, 10
1031 μg/mL heparin, 100nM γ-secretase inhibitor XX, 0.5% ITS-X

1032 Day 21 – Day 28: MCDB 131, 100 nM LDN-193189, 1 μM T3, 10 μM ALK5i II, 10 μM $ZnSO_4$, 10
1033 μg/mL heparin, 1mM N-Acetyl-L-cysteine, 10μM Trolox, 2μM R428 , 0.5% ITS-X

1034

1035 **Characterization of hESC-derived cultures at beta cell stage (day 28)**

1036 *Flow cytometry analysis*

1037 hESC-derived cell aggregates were dissociated into a single-cell suspension with Accutase™
1038 (Innovative Cell Technologies) at 37 °C for 5 min. Accutase™ was quenched with FACS buffer
1039 (0.2% (w/v) BSA in PBS). Cells were then pelleted, fixed, and permeabilized with
1040 Cytofix/Cytoperm Fixation/Permeabilization Solution (BD Biosciences) for 20 min at 4 °C, and

bioRxiv preprint doi: https://doi.org/10.1101/693671; this version posted July 9, 2019. The copyright holder for this preprint (which was not certified by peer review) is the author/funder, who has granted bioRxiv a license to display the preprint in perpetuity. It is made available under aCC-BY-NC-ND 4.0 International license.

1041 washed twice in BD Perm/Wash™ Buffer. We incubated cells with AF647-conjugated mouse anti-
1042 Nkx6.1 (BD Biosciences) and PE-conjugated rabbit anti-INS (Cell Signaling Technology) antibody
1043 in 50 µl BD Perm/Wash™ Buffer for 1 hour at 4 °C. Following three washes in BD Perm/Wash™
1044 Buffer, cells were analyzed on a FACSCanto II (BD Biosciences) cytometer.

1045 *Immunofluorescence staining and quantification of immunofluorescence signal*

1046 hESC-derived cell aggregates were washed twice with PBS and then fixed with 4%
1047 paraformaldehyde in PBS for 30 min at room temperature. Following three washes in PBS,
1048 aggregates were incubated in 30% sucrose at 4 °C overnight, frozen in Optimal Cutting
1049 Temperature Compound (Sakura Finetek USA), and sectioned at 10 µm with a CM3050S cryostat
1050 (Leica). Sections were washed with PBS, permeabilized, and blocked with
1051 Permeabilization/Blocking Buffer for 1 h at room temperature. Primary and secondary antibodies
1052 were diluted in Permeabilization/Blocking Buffer. We incubated sections overnight at 4°C with
1053 primary antibodies, and then secondary antibodies for 30 min at room temperature. The following
1054 primary antibodies were used: mouse anti-NKX6-1 (LifeSpan BioSciences, 1:250), guinea pig
1055 anti-INS (Dako, 1:1000). Secondary antibodies (1:1000) were Cy3-, Alexafluor488-conjugated
1056 antibodies raised in donkey against mouse and guinea pig (Jackson Immuno Research
1057 Laboratories). We acquired images on a Zeiss Axio-Observer-Z1 microscope with a Zeiss
1058 AxioCam digital camera.

1059 *mRNA sequencing*

1060 For each clone, we collected aggregates from two independent batches of differentiation and
1061 lysed them in RLT Buffer. We then extracted total RNA using the RNeasy Micro Kit (QIAGEN)
1062 following the manufacturer's instructions. mRNA libraries were prepared using KAPA mRNA
1063 Hyper Prep kit (KAPA) and single-end 75 bp reads were sequenced using HiSeq4000 (Illumina).
1064 We used STAR (v2.5.3a) to map reads to the hg19 genome, allowing for up to 10 mismatches.
1065 We retained reads aligned uniquely to one genomic location for subsequent analysis. We then
1066 created input count files for DESeq2 with htseq-count from the HTSeq python package (v.0.9.0)
1067 and tested for differential gene expression using DESeq2 (v1.10.1) with default parameters, using
1068 differentiation batch as a technical covariate in our analysis. We considered genes with an
1069 FDR<.1 as significantly differentially expressed.

1070 *Insulin content measurement*

1071 We washed hESC-derived cell aggregates with PBS, resuspended in 50µl of 0.1% SDS TE buffer
1072 and sonicated for 3 cycles of 30 sec on/ 30 sec off each using a Bioruptor on the high setting. We

bioRxiv preprint doi: https://doi.org/10.1101/693671; this version posted July 9, 2019. The copyright holder for this preprint (which was not certified by peer review) is the author/funder, who has granted bioRxiv a license to display the preprint in perpetuity. It is made available under aCC-BY-NC-ND 4.0 International license.

1073 then immersed the lysate in a solution of 2% HCl and 80% ethanol overnight at 4°C and
1074 centrifuged at max speed for 10 min at 4°C. We collected the supernatant and measured insulin
1075 content using a human insulin ELISA kit (ALPCO). We resuspended the pellets in 50µl TE buffer
1076 and measured DNA content with Nanodrop, and normalized insulin content to DNA content.

1077

1078 **Figure Legends**

1079

1080 **Main Figures**

1081

1082 **Figure 1. Pancreatic islet cell type accessible chromatin defined using snATAC-seq.** (a)
1083 Clustering of accessible chromatin profiles from 14,239 pancreatic islet cells identifies 13 distinct
1084 clusters. Cells are plotted using the first two UMAP components, and clusters are assigned cell
1085 type identities based on promoter accessibility of known marker genes for each cell type. (b)
1086 Promoter accessibility in a 1 kb window around the TSS for selected endocrine and non-endocrine
1087 marker genes for each profiled cell. A cell is colored if it had promoter accessibility for the marker
1088 gene listed in the bottom right corner of each subplot, and otherwise is grey. (c) Genome browser
1089 plots showing aggregate read density (scaled to uniform $1x10^5$ read depth, range: 1-10) for cells
1090 within each cell type cluster at hormone gene loci for endocrine islet cell types: *GCG* (alpha), *INS-*
1091 *IGF2* (beta), *SST* (delta), and *PPY* (gamma). The promoter region for each gene is highlighted,
1092 and the number of cells for each cell type cluster is listed in parenthesis. (d) Spearman correlation
1093 between t-statistics of marker genes based on promoter accessibility (snATAC-seq) or gene
1094 expression (scRNA-seq) using the top 100 most specific gene promoters from each islet snATAC-
1095 seq cluster. (e) Normalized chromVAR motif enrichment values for 111 TF sequence motifs that
1096 have variable activity across clusters. We collapsed multiple clusters for each cell type into a
1097 single cluster (e.g. combining beta 1 and beta 2 into a single beta cell cluster). Subtype-specific
1098 motif enrichment is presented in Figure 2. Position weight matrices and names are shown for
1099 sequence motifs for TF families enriched across different endocrine and non-endocrine cell types.
1100 Enrichment z-scores for FOXA1 and PDX1 motifs in each cell are projected onto UMAP
1101 coordinates to the right of the main heatmap.

1102

1103 **Figure 2. Heterogeneity in alpha and beta cell accessible chromatin and regulatory**
1104 **programs.** (a) Gene promoters with significantly differential chromatin accessibility between sub-

bioRxiv preprint doi: https://doi.org/10.1101/693671; this version posted July 9, 2019. The copyright holder for this preprint (which was not certified by peer review) is the author/funder, who has granted bioRxiv a license to display the preprint in perpetuity. It is made available under aCC-BY-NC-ND 4.0 International license.

1105 clusters of alpha cells (left) and beta cells (right). Genes with increased promoter accessibility in
1106 alpha 1 (GCG^{high}) and beta 1 (INS^{high}) sub-clusters include *GCG* (glucagon) for alpha cells and
1107 *INS* (insulin) for beta cells, as well as genes such as *ABCC8, G6PC2, GCK* and *SLC30A8.*
1108 Conversely, genes with increased promoter accessibility in alpha 2 (GCG^{low}) and beta 2 (INS^{low})
1109 sub-clusters include genes such as *FOSL1, FOSL2*, and *ATF3.* (b) Genes with increased
1110 promoter accessibility in the hormone-high (INS^{high}, GCG^{high}) or hormone-low (INS^{low}, GCG^{low})
1111 state of one cell type were significantly enriched for genes with increased hormone-high or
1112 hormone-low activity in the other cell type, respectively (left); Genes with differential promoter
1113 accessibility across alpha and beta cell states were enriched for genes in beta cell subsets (β sub.
1114 1-4) previously identified in an islet single cell gene expression study. (right) **FDR<.01,
1115 *FDR<.10. (c) Gene ontology terms for biological processes related to glucose response and
1116 hormone secretion were enriched in genes with higher promoter accessibility in INS^{high} and
1117 GCG^{high} cells, whereas terms for stress response, insulin signaling and cell cycle were enriched
1118 in genes with higher promoter accessibility in INS^{low} and GCG^{low} cells. (d) Row-normalized
1119 chromVAR enrichments for 111 TF motifs showing variable enrichment across alpha or beta cells.
1120 We observed motifs enriched for different sub-clusters including RFX family members (RFX2-5)
1121 for GCG^{high} alpha and INS^{high} beta cells, and FOS/JUN family members for GCG^{low} alpha and
1122 INS^{low} beta cells. Individual cell enrichment z-scores of a representative RFX (RFX3) and
1123 FOS/JUN (FOS::JUN) motif are plotted on UMAP coordinates, and the violin plots below each
1124 UMAP plot show enrichment values (median: center line, boxplot limits: quartiles) within each
1125 alpha and beta state. (e) Ordering of alpha and beta cells on a trajectory using high *GCG/INS-*
1126 *IGF2* promoter accessibility as the anchor point with Cicero. Plots show cells binned across this
1127 trajectory from left to right, where the top shows the percentage of cells in the hormone-high state
1128 in a given bin, colored bars above the heatmap represent individual cells with their binary clusters
1129 in their positions across each trajectory, and the heatmap shows chromVAR enrichments for
1130 motifs in bins across each trajectory. (f) Motifs in the FOS/JUN family show increasing enrichment
1131 across the alpha and beta cell trajectory. Genes in the FOS/JUN family with promoter accessibility
1132 patterns that match the motif enrichment patterns (Spearman correlation>.9) are highlighted (in
1133 blue and starred).

1134

1135 **Figure 3. Enrichment of islet single cell accessible chromatin for diabetes and related trait**
1136 **genetic association data.** (a) Cell type specific LD score regression enrichment z-scores for
1137 diabetes-related quantitative endophenotypes (top), type 1 and 2 diabetes (middle), and control

bioRxiv preprint doi: https://doi.org/10.1101/693671; this version posted July 9, 2019. The copyright holder for this preprint (which was not certified by peer review) is the author/funder, who has granted bioRxiv a license to display the preprint in perpetuity. It is made available under aCC-BY-NC-ND 4.0 International license.

1138 traits (bottom) for islet snATAC-seq clusters. **FDR<.01 *FDR<.1. (b) Single cell enrichment z-
1139 scores for fasting glucose level, type 2 diabetes, major depressive disorder, and lupus projected
1140 onto UMAP coordinates (left panels), boxplot showing z-score enrichment distribution per cell
1141 type and state (middle panels), and z-score enrichment distribution split into 10 bins based on
1142 beta cell trajectory value (right panels). All boxplots show median (center line) and upper and
1143 lower quartiles (box limits). (c) Genome browser shot of the *DGKB* locus which is associated with
1144 both type 2 diabetes and fasting glucose level. Candidate causal variants fall in an enhancer with
1145 higher accessibility in INS^{high} beta cells and with dynamic chromatin accessibility decreasing
1146 across the beta cell trajectory, consistent with the beta cell enrichment patterns for fasting glucose
1147 level. (d) Correlation between single cell fasting glucose (FG) level enrichments and TF motif
1148 enrichments from chromVAR across all 14.2k cells (left) and 7.2k beta cells (right). Across all
1149 cells, FG level is positively correlated with beta cell TF motifs such as PDX1 and NKX6-1 and
1150 negatively correlated with alpha cell TF motifs such as GATA. Within beta cells, FG level is
1151 positively correlated with TF motifs enriched in the INS^{high} state such as RFX, NRL/MAF, and
1152 FOXA, and negatively correlated with TF motifs enriched in the INS^{low} state such as JUND and
1153 NFE2.

1154

1155 **Figure 4. Genetic variants with islet cell type- and state-specific effects on chromatin**
1156 **accessibility.** (a) Percentage of HRC reference panel r1.1 variants in any endocrine cell type
1157 peak (n=1,411,387 total) that had significant deltaSVM predictions at FDR<.1 for the reference
1158 (ref) or alternate (alt) allele in different endocrine cell types and states. (b) Spearman correlation
1159 comparing deltaSVM score to chromatin accessibility allelic imbalance z-scores using variants
1160 with significant deltaSVM predictions for alpha and beta states. (c) Luciferase gene reporter
1161 assays of five fine-mapped T2D variants with predicted beta cell effects in MIN6 cells. All tested
1162 variants (n=3) had significant effects in gene reporter assays and were directionally consistent
1163 with deltaSVM effects (highlighted with a circle around the allele with higher predicted effect).
1164 Data shown are mean ± 95% confidence interval. Two-sided Student's T-test *P<.05 **P<.01
1165 ***P<.001. (d) Enrichment of ensemble islet caQTLs for SNPs with significant deltaSVM effects
1166 in alpha and beta cells (left) and categorized based on shared, cell type- and state-specific
1167 deltaSVM effects on alpha and beta cells (right). Two-sided Fisher's exact test. ns, not significant.
1168 (e) Variants with predicted cell type- and state-specific effects on alpha and beta cells, where size
1169 indicates magnitude of the deltaSVM z-score and color indicates the effect allele. Ref=blue,
1170 alt=red (left). TF motif families enriched in sequences surrounding the effect allele compared to

bioRxiv preprint doi: https://doi.org/10.1101/693671; this version posted July 9, 2019. The copyright holder for this preprint (which was not certified by peer review) is the author/funder, who has granted bioRxiv a license to display the preprint in perpetuity. It is made available under aCC-BY-NC-ND 4.0 International license.

1171 the non-effect allele for each variant category (middle). Promoter accessibility patterns of genes
1172 in in enriched TF motif families. TFs with promoter accessibility patterns that match TF motif
1173 enrichment patterns are highlighted in blue and starred (right). (f) Enrichment of low frequency
1174 and rare variants with significant effects on islet chromatin for T2D association at different p-value
1175 thresholds. Data shown are enrichment ± 95% confidence interval. Two-sided binomial test
1176 *P<.05. (g) Low-frequency T2D-associated variant rs78840640 at the *IGF2BP3* signal has a high
1177 causal probability (PPA=0.33), overlaps peaks in both beta cell states, and is predicted to have
1178 allelic effects in beta cells.

1179 **Figure 5. Chromatin co-accessibility links cell type enhancers and diabetes risk variants**
1180 **to target genes.** (a) Distance-matched odds that beta cell co-accessibility links overlap islet pcHi-
1181 C chromatin loops at different co-accessibility threshold bins. (b) Beta cell (top) and alpha cell
1182 (middle) co-accessibility between pairs of accessible chromatin sites and high-confidence
1183 promoter capture Hi-C interactions from bulk islets (bottom) anchored at the *PDX1* promoter. (c)
1184 Beta cell co-accessibility anchored on an enhancer within *KCNQ1* harboring causal T2D variant
1185 rs231361 (PPA=1) shows distal links to the *INS* promoter as well as other non-promoter sites.
1186 This enhancer has an accessible peak call in the INS^{high} beta cell state but not the INS^{low} state
1187 and has dynamic accessibility across the beta cell state trajectory. rs231361 disrupts a sequence
1188 motif for *RFX,* which itself is enriched in INS^{high} beta cells, has dynamic enrichment across the
1189 beta cell trajectory, and is predicted to have allelic effects on INS^{high} beta cells (deltaSVM z-score
1190 *FDR<.1). We performed CRISPR/Cas9-mediated deletion of the 2.6 kb genomic region flanking
1191 this enhancer (highlighted in grey) in hESCs ($KCNQ1^{\Delta Enh}$). (d) Differential expression analysis of
1192 genes within 2 Mb of the *KCNQ1* enhancer in beta cell stage cultures (day 28) from $KCNQ1^{\Delta Enh}$
1193 (n=6; 3 clones each differentiated two times) and control (n=2; 1 clone differentiated two times)
1194 hESC clones. *INS* and *CDKN1C* mRNA levels are significantly reduced in $KCNQ1^{\Delta Enh}$ compared
1195 to control cells, while other genes in the region show no significant difference in expression. Data
1196 are shown as transcripts per million (TPM). (e) Representative immunofluorescence staining for
1197 INS (green) and NKX6-1 (red) with DAPI staining (blue) on beta cell stage $KCNQ1^{\Delta Enh}$ and control
1198 aggregates. Scale bar, 50μm. (f) Histogram showing INS fluorescence intensity by flow cytometry
1199 (left panel) and quantification of INS median fluorescence intensity (MFI, right panel) in beta cell
1200 stage cultures from $KCNQ1^{\Delta Enh}$ (n=9; 3 clones each differentiated three times) and control (n=6;
1201 2 clones each differentiated three times) cells. (g) Insulin content in beta cell stage cultures from
1202 $KCNQ1^{\Delta Enh}$ (n=9; 3 clones each differentiated three times) and control (n=6; 2 clones

bioRxiv preprint doi: https://doi.org/10.1101/693671; this version posted July 9, 2019. The copyright holder for this preprint (which was not certified by peer review) is the author/funder, who has granted bioRxiv a license to display the preprint in perpetuity. It is made available under aCC-BY-NC-ND 4.0 International license.

1203 differentiated three times) clones. Data are shown as mean ± SEM. * $p < 0.05$, *** $p<0.001$, ns,
1204 not significant by two-sided Student's T-test.

1205

1206 ## Acknowledgements
1207

1208 This work was supported by NIH R01DK114650 and U01DK105554 (sub-award) to K.G.,
1209 R01DK068471 and U01DK105541 to M.S., U01DK120429 to K.G. and M.S., and by the UC San
1210 Diego School of Medicine to the Center for Epigenomics. Data from the UK Biobank was accessed
1211 under application 24058. We thank Ileana Matta for preparation of RNA-seq libraries.

1212

1213 ## Conflict of Interest
1214

1215 The authors have no conflict of interest to disclose.

1216

1217 ## Author Contributions
1218

1219 K.J.G., D.U.G, and M.Sa. conceived of and supervised the research in the study; K.J.G., D.U.G.,
1220 M.Sa., J.C., C.Z, and Z.C. wrote the manuscript; J.C. performed analyses of single cell and
1221 genetic data; C.Z., M.Sc and J.W. performed hESC experiments; Z.C. performed analyses of
1222 single cell data; J.Y.H. performed single cell assays and genotyping; S.H., A.D. and M.O.
1223 performed reporter experiments; Y.Q. performed analyses of 4C data; Y.Sui performed analyses
1224 of hESC data; Y.Sun and P.K. developed and processed data for the epigenome database; R.F.
1225 contributed analyses of single cell data; S.P. contributed to the development of single cell assays.

1226

1227 ## Data Availability
1228

1229 Processed data and annotations will be made available at www.t2depigenome.org, and raw
1230 sequence data will be deposited in GEO prior to publication. All other source data are either
1231 included in the study or available from the corresponding authors upon request.

1232

bioRxiv preprint doi: https://doi.org/10.1101/693671; this version posted July 9, 2019. The copyright holder for this preprint (which was not certified by peer review) is the author/funder, who has granted bioRxiv a license to display the preprint in perpetuity. It is made available under aCC-BY-NC-ND 4.0 International license.

1233 **References**
1234

1235 1. Maurano, M. T. *et al.* Systematic Localization of Common Disease-Associated Variation in
1236 Regulatory DNA. *Science* **337**, 1190–1195 (2012).
1237 2. Cusanovich, D. A. *et al.* Multiplex Single Cell Profiling of Chromatin Accessibility by
1238 Combinatorial Cellular Indexing. *Science* **348**, 910–914 (2015).
1239 3. Buenrostro, J. D. *et al.* Single-cell chromatin accessibility reveals principles of regulatory
1240 variation. *Nature* **523**, 486–490 (2015).
1241 4. Preissl, S. *et al.* Single-nucleus analysis of accessible chromatin in developing mouse
1242 forebrain reveals cell-type-specific transcriptional regulation. *Nat. Neurosci.* **21**, 432–439
1243 (2018).
1244 5. Cusanovich, D. A. *et al.* A Single-Cell Atlas of In Vivo Mammalian Chromatin Accessibility.
1245 *Cell* **174**, 1309–1324.e18 (2018).
1246 6. Pliner, H. A. *et al.* Cicero Predicts cis-Regulatory DNA Interactions from Single-Cell
1247 Chromatin Accessibility Data. *Mol. Cell* **71**, 858–871.e8 (2018).
1248 7. Litzenburger, U. M. *et al.* Single-cell epigenomic variability reveals functional cancer
1249 heterogeneity. *Genome Biol.* **18**, 15 (2017).
1250 8. Buenrostro, J. D. *et al.* Integrated Single-Cell Analysis Maps the Continuous Regulatory
1251 Landscape of Human Hematopoietic Differentiation. *Cell* **173**, 1535–1548.e16 (2018).
1252 9. Ulirsch, J. C. *et al.* Interrogation of human hematopoiesis at single-cell and single-variant
1253 resolution. *Nat. Genet.* **51**, 683–693 (2019).
1254 10. Mahajan, A. *et al.* Fine-mapping type 2 diabetes loci to single-variant resolution using
1255 high-density imputation and islet-specific epigenome maps. *Nat. Genet.* **50**, 1505–1513
1256 (2018).

bioRxiv preprint doi: https://doi.org/10.1101/693671; this version posted July 9, 2019. The copyright holder for this preprint (which was not certified by peer review) is the author/funder, who has granted bioRxiv a license to display the preprint in perpetuity. It is made available under aCC-BY-NC-ND 4.0 International license.

1257 11. Wood, A. R. *et al.* A Genome-Wide Association Study of IVGTT-Based Measures of
1258 First-Phase Insulin Secretion Refines the Underlying Physiology of Type 2 Diabetes Variants.
1259 *Diabetes* **66**, 2296–2309 (2017).
1260 12. Morris, A. P. *et al.* Large-scale association analysis provides insights into the genetic
1261 architecture and pathophysiology of type 2 diabetes. *Nat. Genet.* **44**, 981–990 (2012).
1262 13. Dupuis, J. *et al.* New genetic loci implicated in fasting glucose homeostasis and their
1263 impact on type 2 diabetes risk. *Nat. Genet.* **42**, 105–116 (2010).
1264 14. Thurner, M. *et al.* Integration of human pancreatic islet genomic data refines regulatory
1265 mechanisms at Type 2 Diabetes susceptibility loci. *eLife* **7**,
1266 15. Fuchsberger, C. *et al.* The genetic architecture of type 2 diabetes. *Nature* **536**, 41–47
1267 (2016).
1268 16. Gaulton, K. J. *et al.* Genetic fine mapping and genomic annotation defines causal
1269 mechanisms at type 2 diabetes susceptibility loci. *Nat. Genet.* **47**, 1415–1425 (2015).
1270 17. Pasquali, L. *et al.* Pancreatic islet enhancer clusters enriched in type 2 diabetes risk-
1271 associated variants. *Nat. Genet.* **46**, 136–143 (2014).
1272 18. Gaulton, K. J. *et al.* A map of open chromatin in human pancreatic islets. *Nat. Genet.* **42**,
1273 255–259 (2010).
1274 19. van der Meulen, T. *et al.* Urocortin3 mediates somatostatin-dependent negative
1275 feedback control of insulin secretion. *Nat. Med.* **21**, 769–776 (2015).
1276 20. Caicedo, A. Paracrine and autocrine interactions in the human islet: more than meets
1277 the eye. *Semin. Cell Dev. Biol.* **24**, 11–21 (2013).
1278 21. DiGruccio, M. R. *et al.* Comprehensive alpha, beta and delta cell transcriptomes reveal
1279 that ghrelin selectively activates delta cells and promotes somatostatin release from
1280 pancreatic islets. *Mol. Metab.* **5**, 449–458 (2016).
1281 22. Dorrell, C. *et al.* Human islets contain four distinct subtypes of β cells. *Nat. Commun.* **7**,
1282 ncomms11756 (2016).

bioRxiv preprint doi: https://doi.org/10.1101/693671; this version posted July 9, 2019. The copyright holder for this preprint (which was not certified by peer review) is the author/funder, who has granted bioRxiv a license to display the preprint in perpetuity. It is made available under aCC-BY-NC-ND 4.0 International license.

1283 23. Xin, Y. *et al.* Pseudotime Ordering of Single Human β-Cells Reveals States of Insulin
1284 Production and Unfolded Protein Response. *Diabetes* db180365 (2018). doi:10.2337/db18-
1285 0365
1286 24. Korsunsky, I. *et al.* Fast, sensitive, and accurate integration of single cell data with
1287 Harmony. *bioRxiv* 461954 (2018). doi:10.1101/461954
1288 25. Bader, E. *et al.* Identification of proliferative and mature β-cells in the islets of
1289 Langerhans. *Nature* **535**, 430–434 (2016).
1290 26. Liu, J. S. E. & Hebrok, M. All mixed up: defining roles for β-cell subtypes in mature islets.
1291 *Genes Dev.* **31**, 228–240 (2017).
1292 27. Greenwald, W. W. *et al.* Pancreatic islet chromatin accessibility and conformation
1293 defines distal enhancer networks of type 2 diabetes risk. *bioRxiv* 299388 (2018).
1294 doi:10.1101/299388
1295 28. Varshney, A. *et al.* Genetic regulatory signatures underlying islet gene expression and
1296 type 2 diabetes. *Proc. Natl. Acad. Sci. U. S. A.* **114**, 2301–2306 (2017).
1297 29. Khetan, S. *et al.* Type 2 Diabetes-Associated Genetic Variants Regulate Chromatin
1298 Accessibility in Human Islets. *Diabetes* **67**, 2466–2477 (2018).
1299 30. Haghverdi, L., Lun, A. T. L., Morgan, M. D. & Marioni, J. C. Batch effects in single-cell
1300 RNA-sequencing data are corrected by matching mutual nearest neighbors. *Nat. Biotechnol.*
1301 **36**, 421–427 (2018).
1302 31. Segerstolpe, Å. *et al.* Single-Cell Transcriptome Profiling of Human Pancreatic Islets in
1303 Health and Type 2 Diabetes. *Cell Metab.* **24**, 593–607 (2016).
1304 32. Baron, M. *et al.* A Single-Cell Transcriptomic Map of the Human and Mouse Pancreas
1305 Reveals Inter- and Intra-cell Population Structure. *Cell Syst.* **3**, 346–360.e4 (2016).
1306 33. George, D., Ahrens, P. & Lambert, S. Satellite glial cells represent a population of
1307 developmentally arrested Schwann cells. *Glia* **66**, 1496–1506 (2018).

bioRxiv preprint doi: https://doi.org/10.1101/693671; this version posted July 9, 2019. The copyright holder for this preprint (which was not certified by peer review) is the author/funder, who has granted bioRxiv a license to display the preprint in perpetuity. It is made available under aCC-BY-NC-ND 4.0 International license.

1308 34. Galvagni, F. *et al.* CD93 and dystroglycan cooperation in human endothelial cell
1309 adhesion and migration adhesion and migration. *Oncotarget* **7**, 10090–10103 (2016).
1310 35. Ackermann, A. M., Wang, Z., Schug, J., Naji, A. & Kaestner, K. H. Integration of ATAC-
1311 seq and RNA-seq identifies human alpha cell and beta cell signature genes. *Mol. Metab.* **5**,
1312 233–244 (2016).
1313 36. Arda, H. E. *et al.* A Chromatin Basis for Cell Lineage and Disease Risk in the Human
1314 Pancreas. *Cell Syst.* **7**, 310–322.e4 (2018).
1315 37. Schep, A. N., Wu, B., Buenrostro, J. D. & Greenleaf, W. J. chromVAR: inferring
1316 transcription-factor-associated accessibility from single-cell epigenomic data. *Nat. Methods*
1317 **14**, 975–978 (2017).
1318 38. Khan, A. *et al.* JASPAR 2018: update of the open-access database of transcription
1319 factor binding profiles and its web framework. *Nucleic Acids Res.* **46**, D1284 (2018).
1320 39. Wilson, M. E., Scheel, D. & German, M. S. Gene expression cascades in pancreatic
1321 development. *Mech. Dev.* **120**, 65–80 (2003).
1322 40. Conrad, E. *et al.* The MAFB transcription factor impacts islet α-cell function in rodents
1323 and represents a unique signature of primate islet β-cells. *Am. J. Physiol. Endocrinol. Metab.*
1324 **310**, E91–E102 (2016).
1325 41. Katoh, M. C. *et al.* MafB Is Critical for Glucagon Production and Secretion in Mouse
1326 Pancreatic α Cells In Vivo. *Mol. Cell. Biol.* **38**, (2018).
1327 42. Nishimura, W., Takahashi, S. & Yasuda, K. MafA is critical for maintenance of the
1328 mature beta cell phenotype in mice. *Diabetologia* **58**, 566–574 (2015).
1329 43. Ozato, K., Tailor, P. & Kubota, T. The interferon regulatory factor family in host defense:
1330 mechanism of action. *J. Biol. Chem.* **282**, 20065–20069 (2007).
1331 44. De Val, S. & Black, B. L. Transcriptional Control of Endothelial Cell Development. *Dev.*
1332 *Cell* **16**, 180–195 (2009).

bioRxiv preprint doi: https://doi.org/10.1101/693671; this version posted July 9, 2019. The copyright holder for this preprint (which was not certified by peer review) is the author/funder, who has granted bioRxiv a license to display the preprint in perpetuity. It is made available under aCC-BY-NC-ND 4.0 International license.

1333 45. Lawlor, N. *et al.* Single-cell transcriptomes identify human islet cell signatures and reveal
1334 cell-type–specific expression changes in type 2 diabetes. *Genome Res.* **27**, 208–222 (2017).
1335 46. Bahrami, S. & Drabløs, F. Gene regulation in the immediate-early response process.
1336 *Adv. Biol. Regul.* **62**, 37–49 (2016).
1337 47. Trapnell, C. *et al.* Pseudo-temporal ordering of individual cells reveals dynamics and
1338 regulators of cell fate decisions. *Nat. Biotechnol.* **32**, 381 (2014).
1339 48. Wingender, E., Schoeps, T., Haubrock, M. & Dönitz, J. TFClass: a classification of
1340 human transcription factors and their rodent orthologs. *Nucleic Acids Res.* **43**, D97-102
1341 (2015).
1342 49. Ait-Lounis, A. *et al.* The transcription factor Rfx3 regulates beta-cell differentiation,
1343 function, and glucokinase expression. *Diabetes* **59**, 1674–1685 (2010).
1344 50. Chandra, V. *et al.* RFX6 regulates insulin secretion by modulating Ca2+ homeostasis in
1345 human β cells. *Cell Rep.* **9**, 2206–2218 (2014).
1346 51. Piccand, J. *et al.* Rfx6 Maintains the Functional Identity of Adult Pancreatic β Cells. *Cell*
1347 *Rep.* **9**, 2219–2232 (2014).
1348 52. Hindorff, L. A. *et al.* Potential etiologic and functional implications of genome-wide
1349 association loci for human diseases and traits. *Proc. Natl. Acad. Sci. U. S. A.* **106**, 9362–
1350 9367 (2009).
1351 53. Parker, S. C. J. *et al.* Chromatin stretch enhancer states drive cell-specific gene
1352 regulation and harbor human disease risk variants. *Proc. Natl. Acad. Sci. U. S. A.* **110**,
1353 17921–17926 (2013).
1354 54. Aylward, A., Chiou, J., Okino, M.-L., Kadakia, N. & Gaulton, K. J. Shared genetic risk
1355 contributes to type 1 and type 2 diabetes etiology. *Hum. Mol. Genet.* (2018).
1356 doi:10.1093/hmg/ddy314

bioRxiv preprint doi: https://doi.org/10.1101/693671; this version posted July 9, 2019. The copyright holder for this preprint (which was not certified by peer review) is the author/funder, who has granted bioRxiv a license to display the preprint in perpetuity. It is made available under aCC-BY-NC-ND 4.0 International license.

1357 55. Strawbridge, R. J. *et al.* Genome-wide association identifies nine common variants
1358 associated with fasting proinsulin levels and provides new insights into the pathophysiology
1359 of type 2 diabetes. *Diabetes* **60**, 2624–2634 (2011).
1360 56. Manning, A. K. *et al.* A genome-wide approach accounting for body mass index identifies
1361 genetic variants influencing fasting glycemic traits and insulin resistance. *Nat. Genet.* **44**,
1362 659–669 (2012).
1363 57. Locke, A. E. *et al.* Genetic studies of body mass index yield new insights for obesity
1364 biology. *Nature* **518**, 197–206 (2015).
1365 58. Saxena, R. *et al.* Genetic variation in GIPR influences the glucose and insulin responses
1366 to an oral glucose challenge. *Nat. Genet.* **42**, 142–148 (2010).
1367 59. Wheeler, E. *et al.* Impact of common genetic determinants of Hemoglobin A1c on type 2
1368 diabetes risk and diagnosis in ancestrally diverse populations: A transethnic genome-wide
1369 meta-analysis. *PLoS Med.* **14**, e1002383 (2017).
1370 60. Hou, L. *et al.* Genome-wide association study of 40,000 individuals identifies two novel
1371 loci associated with bipolar disorder. *Hum. Mol. Genet.* **25**, 3383–3394 (2016).
1372 61. Schizophrenia Working Group of the Psychiatric Genomics Consortium. Biological
1373 insights from 108 schizophrenia-associated genetic loci. *Nature* **511**, 421–427 (2014).
1374 62. de Lange, K. M. *et al.* Genome-wide association study implicates immune activation of
1375 multiple integrin genes in inflammatory bowel disease. *Nat. Genet.* **49**, 256–261 (2017).
1376 63. Bentham, J. *et al.* Genetic association analyses implicate aberrant regulation of innate
1377 and adaptive immunity genes in the pathogenesis of systemic lupus erythematosus. *Nat.*
1378 *Genet.* **47**, 1457–1464 (2015).
1379 64. Jin, Y. *et al.* Genome-wide association studies of autoimmune vitiligo identify 23 new risk
1380 loci and highlight key pathways and regulatory variants. *Nat. Genet.* **48**, 1418–1424 (2016).
1381 65. Cordell, H. J. *et al.* International genome-wide meta-analysis identifies new primary
1382 biliary cirrhosis risk loci and targetable pathogenic pathways. *Nat. Commun.* **6**, 8019 (2015).

bioRxiv preprint doi: https://doi.org/10.1101/693671; this version posted July 9, 2019. The copyright holder for this preprint (which was not certified by peer review) is the author/funder, who has granted bioRxiv a license to display the preprint in perpetuity. It is made available under aCC-BY-NC-ND 4.0 International license.

1383 66. Wray, N. R. *et al.* Genome-wide association analyses identify 44 risk variants and refine
1384 the genetic architecture of major depression. *Nat. Genet.* **50**, 668–681 (2018).
1385 67. Lambert, J. C. *et al.* Meta-analysis of 74,046 individuals identifies 11 new susceptibility
1386 loci for Alzheimer's disease. *Nat. Genet.* **45**, 1452–1458 (2013).
1387 68. Finucane, H. K. *et al.* Partitioning heritability by functional annotation using genome-wide
1388 association summary statistics. *Nat. Genet.* **47**, 1228–1235 (2015).
1389 69. Bulik-Sullivan, B. K. *et al.* LD Score regression distinguishes confounding from
1390 polygenicity in genome-wide association studies. *Nat. Genet.* **47**, 291–295 (2015).
1391 70. Lee, D. *et al.* A method to predict the impact of regulatory variants from DNA sequence.
1392 *Nat. Genet.* **47**, 955–961 (2015).
1393 71. 1000 Genomes Project Consortium *et al.* A global reference for human genetic variation.
1394 *Nature* **526**, 68–74 (2015).
1395 72. Khetan, S. *et al.* Chromatin accessibility profiling uncovers genetic- and T2D disease
1396 state-associated changes in cis-regulatory element use in human islets. *bioRxiv* 192922
1397 (2017). doi:10.1101/192922
1398 73. Shlyueva, D., Stampfel, G. & Stark, A. Transcriptional enhancers: from properties to
1399 genome-wide predictions. *Nat. Rev. Genet.* **15**, 272–286 (2014).
1400 74. Schmitt, A. D., Hu, M. & Ren, B. Genome-wide mapping and analysis of chromosome
1401 architecture. *Nat. Rev. Mol. Cell Biol.* **17**, 743–755 (2016).
1402 75. Thurman, R. E. *et al.* The accessible chromatin landscape of the human genome. *Nature*
1403 **489**, 75–82 (2012).
1404 76. Miguel-Escalada, I. *et al.* Human pancreatic islet 3D chromatin architecture provides
1405 insights into the genetics of type 2 diabetes. *bioRxiv* 400291 (2018). doi:10.1101/400291
1406 77. Jian, X. & Felsenfeld, G. Insulin promoter in human pancreatic β cells contacts diabetes
1407 susceptibility loci and regulates genes affecting insulin metabolism. *Proc. Natl. Acad. Sci. U.*
1408 *S. A.* **115**, E4633–E4641 (2018).

bioRxiv preprint doi: https://doi.org/10.1101/693671; this version posted July 9, 2019. The copyright holder for this preprint (which was not certified by peer review) is the author/funder, who has granted bioRxiv a license to display the preprint in perpetuity. It is made available under aCC-BY-NC-ND 4.0 International license.

1409 78. Holmkvist, J. *et al.* The type 2 diabetes associated minor allele of rs2237895 KCNQ1
1410 associates with reduced insulin release following an oral glucose load. *PloS One* **4**, e5872
1411 (2009).
1412 79. Jonsson, A. *et al.* A variant in the KCNQ1 gene predicts future type 2 diabetes and
1413 mediates impaired insulin secretion. *Diabetes* **58**, 2409–2413 (2009).
1414 80. Tan, J. T. *et al.* Genetic Variation in KCNQ1 Associates With Fasting Glucose andβ-Cell
1415 Function. *Diabetes* **58**, 1445–1449 (2009).
1416 81. Yasuda, K. *et al.* Variants in KCNQ1 are associated with susceptibility to type 2 diabetes
1417 mellitus. *Nat. Genet.* **40**, 1092–1097 (2008).
1418 82. Kanai, M. *et al.* Genetic analysis of quantitative traits in the Japanese population links
1419 cell types to complex human diseases. *Nat. Genet.* **50**, 390–400 (2018).
1420 83. Rezania, A. *et al.* Reversal of diabetes with insulin-producing cells derived in vitro from
1421 human pluripotent stem cells. *Nat. Biotechnol.* **32**, 1121–1133 (2014).
1422 84. Suzuki, K. *et al.* Identification of 28 new susceptibility loci for type 2 diabetes in the
1423 Japanese population. *Nat. Genet.* **51**, 379–386 (2019).
1424 85. Claussnitzer, M. *et al.* FTO Obesity Variant Circuitry and Adipocyte Browning in
1425 Humans. *N. Engl. J. Med.* **373**, 895–907 (2015).
1426 86. Fogarty, M. P., Cannon, M. E., Vadlamudi, S., Gaulton, K. J. & Mohlke, K. L.
1427 Identification of a regulatory variant that binds FOXA1 and FOXA2 at the CDC123/CAMK1D
1428 type 2 diabetes GWAS locus. *PLoS Genet.* **10**, e1004633 (2014).
1429 87. Rusu, V. *et al.* Type 2 Diabetes Variants Disrupt Function of SLC16A11 through Two
1430 Distinct Mechanisms. *Cell* **170**, 199–212.e20 (2017).
1431 88. Carrat, G. R. *et al.* Decreased STARD10 Expression Is Associated with Defective Insulin
1432 Secretion in Humans and Mice. *Am. J. Hum. Genet.* **100**, 238–256 (2017).
1433 89. Claussnitzer, M. *et al.* Leveraging cross-species transcription factor binding site patterns:
1434 from diabetes risk loci to disease mechanisms. *Cell* **156**, 343–358 (2014).

bioRxiv preprint doi: https://doi.org/10.1101/693671; this version posted July 9, 2019. The copyright holder for this preprint (which was not certified by peer review) is the author/funder, who has granted bioRxiv a license to display the preprint in perpetuity. It is made available under aCC-BY-NC-ND 4.0 International license.

1435 90. Roman, T. S. *et al.* A Type 2 Diabetes-Associated Functional Regulatory Variant in a
1436 Pancreatic Islet Enhancer at the Adcy5 Locus. *Diabetes* db170464 (2017). doi:10.2337/db17-
1437 0464
1438 91. Kycia, I. *et al.* A Common Type 2 Diabetes Risk Variant Potentiates Activity of an
1439 Evolutionarily Conserved Islet Stretch Enhancer and Increases C2CD4A and C2CD4B
1440 Expression. *Am. J. Hum. Genet.* **102**, 620–635 (2018).
1441 92. Steck, A. K. & Rewers, M. J. Genetics of Type 1 Diabetes. *Clin. Chem.* **57**, 176–185
1442 (2011).
1443 93. Yang, Y. & Chan, L. Monogenic Diabetes: What It Teaches Us on the Common Forms of
1444 Type 1 and Type 2 Diabetes. *Endocr. Rev.* **37**, 190–222 (2016).
1445 94. Camunas-Soler, J. *et al.* Pancreas patch-seq links physiologic dysfunction in diabetes to
1446 single-cell transcriptomic phenotypes. *bioRxiv* 555110 (2019). doi:10.1101/555110
1447 95. Avrahami, D., Klochendler, A., Dor, Y. & Glaser, B. Beta cell heterogeneity: an evolving
1448 concept. *Diabetologia* **60**, 1363–1369 (2017).
1449 96. Picelli, S. *et al.* Tn5 transposase and tagmentation procedures for massively scaled
1450 sequencing projects. *Genome Res.* **24**, 2033–2040 (2014).
1451 97. Li, H. & Durbin, R. Fast and accurate long-read alignment with Burrows-Wheeler
1452 transform. *Bioinforma. Oxf. Engl.* **26**, 589–595 (2010).
1453 98. Li, H. *et al.* The Sequence Alignment/Map format and SAMtools. *Bioinforma. Oxf. Engl.*
1454 **25**, 2078–2079 (2009).
1455 99. Wolf, F. A., Angerer, P. & Theis, F. J. SCANPY: large-scale single-cell gene expression
1456 data analysis. *Genome Biol.* **19**, 15 (2018).
1457 100. Zhang, Y. *et al.* Model-based analysis of ChIP-Seq (MACS). *Genome Biol.* **9**, R137
1458 (2008).
1459 101. ENCODE Project Consortium. An integrated encyclopedia of DNA elements in the
1460 human genome. *Nature* **489**, 57–74 (2012).

bioRxiv preprint doi: https://doi.org/10.1101/693671; this version posted July 9, 2019. The copyright holder for this preprint (which was not certified by peer review) is the author/funder, who has granted bioRxiv a license to display the preprint in perpetuity. It is made available under aCC-BY-NC-ND 4.0 International license.

1461 102. Quinlan, A. R. & Hall, I. M. BEDTools: a flexible suite of utilities for comparing genomic
1462 features. *Bioinformatics* **26**, 841–842 (2010).
1463 103. Kuleshov, M. V. *et al.* Enrichr: a comprehensive gene set enrichment analysis web
1464 server 2016 update. *Nucleic Acids Res.* **44**, W90-97 (2016).
1465 104. Subramanian, A. *et al.* Gene set enrichment analysis: a knowledge-based approach for
1466 interpreting genome-wide expression profiles. *Proc. Natl. Acad. Sci. U. S. A.* **102**, 15545–
1467 15550 (2005).
1468 105. Finucane, H. K. *et al.* Heritability enrichment of specifically expressed genes identifies
1469 disease-relevant tissues and cell types. *Nat. Genet.* **50**, 621–629 (2018).
1470 106. Li, Y. I. *et al.* RNA splicing is a primary link between genetic variation and disease.
1471 *Science* **352**, 600–604 (2016).
1472 107. McCarthy, S. *et al.* A reference panel of 64,976 haplotypes for genotype imputation. *Nat.*
1473 *Genet.* **48**, 1279–1283 (2016).
1474 108. Das, S. *et al.* Next-generation genotype imputation service and methods. *Nat. Genet.* **48**,
1475 1284–1287 (2016).
1476 109. van de Geijn, B., McVicker, G., Gilad, Y. & Pritchard, J. K. WASP: allele-specific
1477 software for robust molecular quantitative trait locus discovery. *Nat. Methods* **12**, 1061–1063
1478 (2015).
1479 110. Bailey, T. L. *et al.* MEME SUITE: tools for motif discovery and searching. *Nucleic Acids*
1480 *Res.* **37**, W202-208 (2009).
1481 111. Raviram, R. *et al.* 4C-ker: A Method to Reproducibly Identify Genome-Wide Interactions
1482 Captured by 4C-Seq Experiments. *PLoS Comput. Biol.* **12**, e1004780 (2016).
1483 112. Langmead, B. & Salzberg, S. L. Fast gapped-read alignment with Bowtie 2. *Nat.*
1484 *Methods* **9**, 357–359 (2012).
1485

bioRxiv preprint doi: https://doi.org/10.1101/693671; this version posted July 9, 2019. The copyright holder for this preprint (which was not certified by peer review) is the author/funder, who has granted bioRxiv a license to display the preprint in perpetuity. It is made available under aCC-BY-NC-ND 4.0 International license.

Figure 1

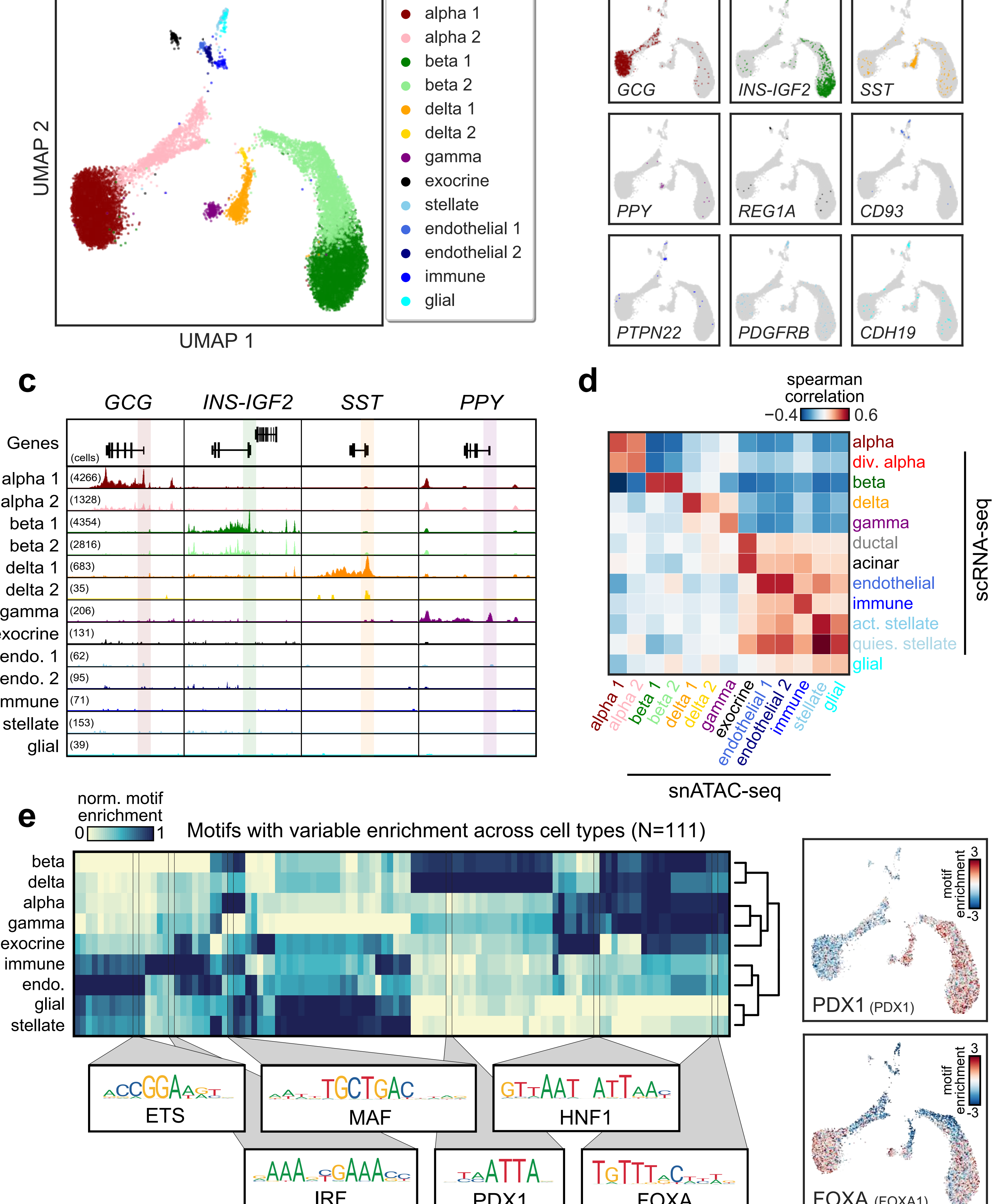

bioRxiv preprint doi: https://doi.org/10.1101/693671; this version posted July 9, 2019. The copyright holder for this preprint (which was not certified by peer review) is the author/funder, who has granted bioRxiv a license to display the preprint in perpetuity. It is made available under aCC-BY-NC-ND 4.0 International license.

Figure 2

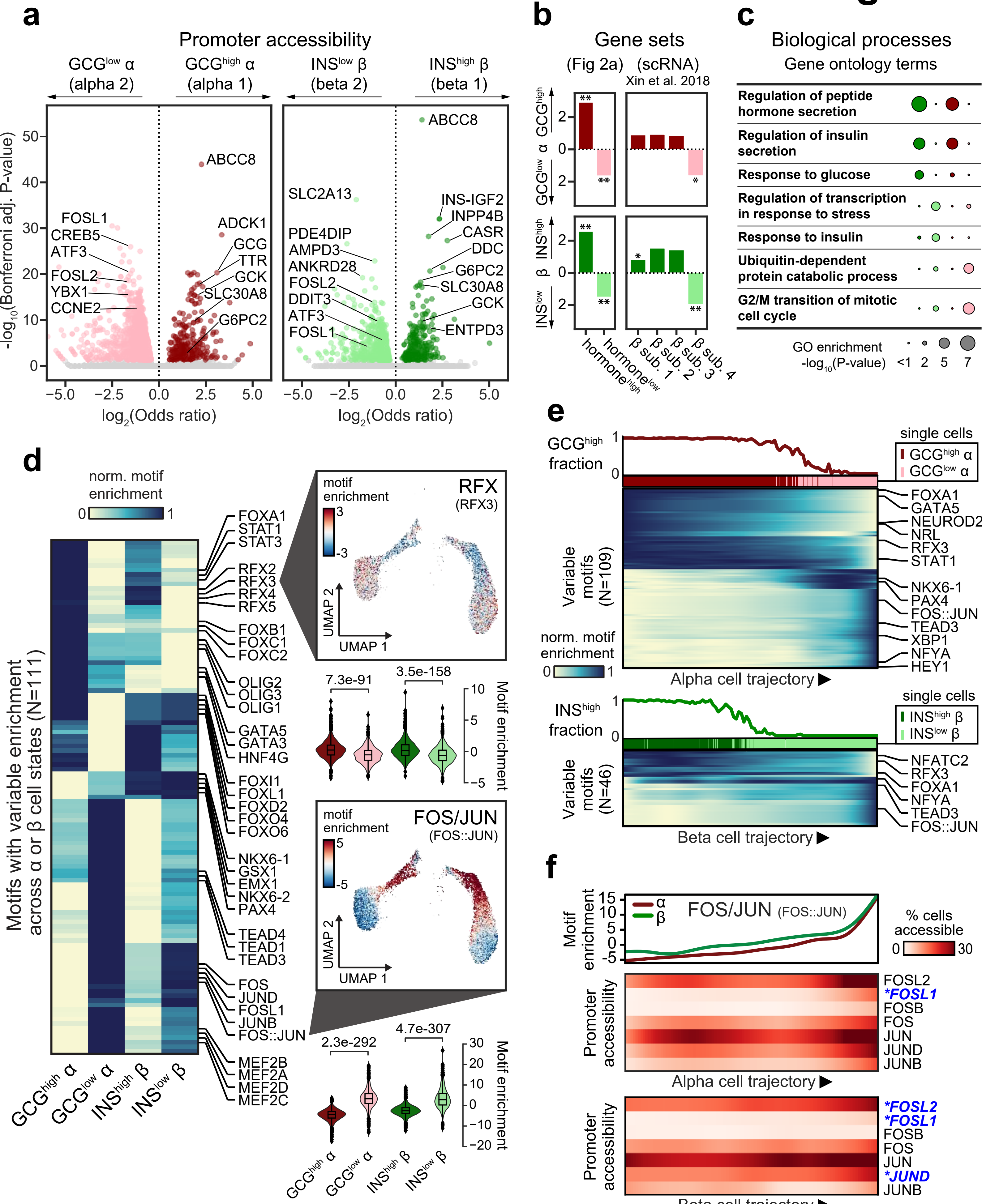

bioRxiv preprint doi: https://doi.org/10.1101/693671; this version posted July 9, 2019. The copyright holder for this preprint (which was not certified by peer review) is the author/funder, who has granted bioRxiv a license to display the preprint in perpetuity. It is made available under a CC-BY-NC-ND 4.0 International license.

Figure 3

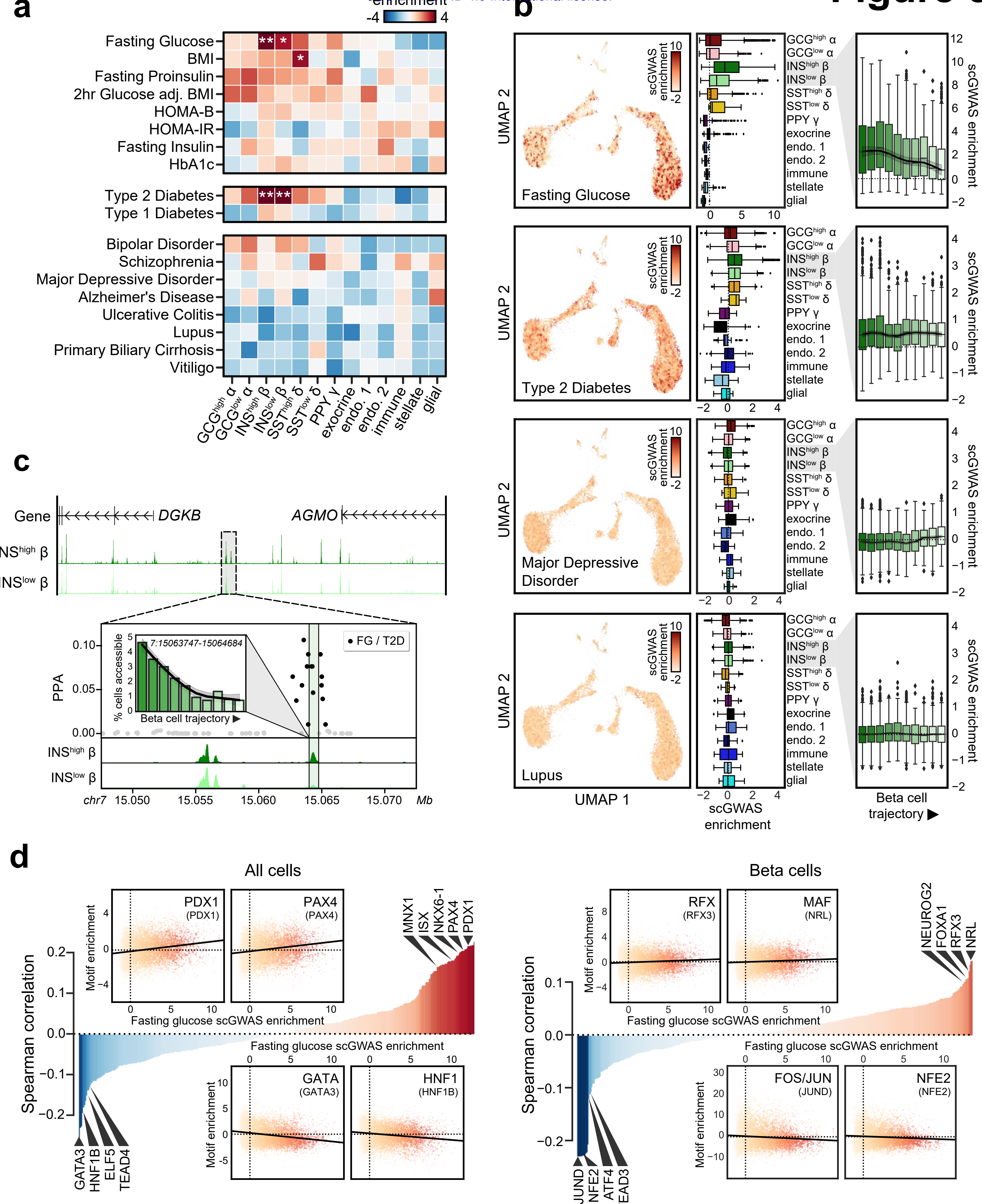

bioRxiv preprint doi: https://doi.org/10.1101/693671; this version posted July 9, 2019. The copyright holder for this preprint (which was not certified by peer review) is the author/funder, who has granted bioRxiv a license to display the preprint in perpetuity. It is made available under aCC-BY-NC-ND 4.0 International license.

Figure 4

a

ns | ref. allele | alt. allele

GCG^high α, GCG^low α, INS^high β, INS^low β, SST^high δ, SST^low δ, PPY γ

0 25 50 75 100

% of HRC variants in endocrine peaks with significant predicted effect

b

Chromatin accessibility allelic imbalance z-score

ρ=0.261 GCG^high α
ρ=0.285 INS^high β
ρ=0.225 GCG^low α
ρ=0.297 INS^low β

4 0 −4

−15 0 15

deltaSVM z-score

c

Relative luciferase activity

ref. allele | alt. allele

1.3e-2, 6.8e-4, 7.3e-3, 2.6e-3, 4.9e-2

Beta cell deltaSVM

A G | A G | T A | C G | T C

rs7482891 *TH*
rs34584161 *RNF6*
rs17712208 *PROX1-AS1*
rs78840640 *IGF2BP3*
rs4679370 *SLC12A8*

d

Islet caQTLs

% with deltaSVM effect

1.64e-66

observed, expected

Islet caQTLs with deltaSVM effect

% within category

observed | expected

8.57e-67, ns, ns, 3.69e-02, ns

shared, high hormone, low hormone, alpha, beta

e

Delta SVM Predictions

high hormone (n=15,769): rs139298684, rs577109679, rs574609810, rs368143450, rs10887077

low hormone (n=12,471): rs74056798, rs1223678, rs35382979, rs189181843, rs188059693

alpha (n=10,564): rs558533167, rs3796635, rs148714451, rs116587033, rs543810540

beta (n=12,833): rs9957371, rs6750361, rs531305149, rs3819100, rs1889903

deltaSVM z-score: 1, 5, >10

higher effect allele: ref. alt.

GCG^high GCG^low INS^high INS^low — α β

Enriched TF Motifs

Motif	$-\log_{10}(P)$
NEUROD1	(59.2)
FOXA1	(56.0)
Mafb	(50.3)
Rfx1	(20.6)
JUND	(107.6)
BACH2	(50.5)
CREB1	(46.8)
E2F4	(39.2)
ELF5	(31.3)
GATA2	(24.8)
ELK4	(23.6)
FOXA1	(23.5)
NEUROD1	(33.3)
FOXA1	(31.9)
NKX6-1	(17.0)
PDX1	(13.0)

Promoter Accessibility

RFX1, *RFX2*, *RFX3*, *RFX4*, *RFX5*, ***RFX6**

ATF1, ***CREB1**, *CREM*

GATA2, *GATA3*, *GATA4*, ***GATA6**

***NKX6-1**, *NKX6-2*, ***NKX6-3**

norm. promoter accessibility 0 1

GCG^high GCG^low INS^high INS^low — α β

f

Low freq. variants with deltaSVM effect

alpha, beta, delta, gamma, endocrine

Enrichment

T2D GWAS P-value: 10^3 10^4 10^5 10^6 10^7 10^8

g

IGF2BP3

rs78840640
MAF = 2.13%

deltaSVM: GCG^high α, GCG^low α, INS^high β, INS^low β

T2D PPA

GCG^high α, GCG^low α, INS^high β, INS^low β

chr7 23.40 23.45 23.50 *Mb*

bioRxiv preprint doi: https://doi.org/10.1101/693671; this version posted July 9, 2019. The copyright holder for this preprint (which was not certified by peer review) is the author/funder, who has granted bioRxiv a license to display the preprint in perpetuity. It is made available under aCC-BY-NC-ND 4.0 International license.

Figure 5